X−ray spectral properties of dust−obscured galaxies in the XMM−SERVS coverage of the XMM-LSS field

Abhijit Kayal [ID],[1,2]⋆ Veeresh Singh [ID],[1]

[1] *Physical Research Laboratory, Navrangpura, Ahmedabad, Gujarat-380 009, India*
[2] *Indian Institute of Technology Gandhinagar, Palaj, Gandhinagar, Gujarat-382 355, India*

ABSTRACT

With an aim to unveil the population of obscured AGN hosted in high−z dust−obscured galaxies (DOGs), we performed X-ray spectral study of 34 DOGs ($0.59 \leq z \leq 4.65$) lying within 5.3 deg^2 of the XMM−SERVS coverage in the XMM-LSS field. To improve the spectral quality of individual sources, we combined all the existing *XMM−Newton* data and also included *Chandra*/ACIS data, whenever available. We find that the X-ray spectra of our DOGs can be fitted with a simple absorbed power law or with a physically-motivated BORUS02 model. The line-of-sight column densities (N_H) in our sources span across a wide range (1.02×10^{22} cm$^{-2} \leq N_H \leq 1.21 \times 10^{24}$ cm^{-2}), with a substantial fraction (~ 17.6 per cent) of them being heavily obscured ($N_H \geq 10^{23}$ cm^{-2}). We also identified one new CT-AGN candidate, yielding the CT-AGN fraction in our sample to be only 3 per cent. The absorption-corrected 2.0−10 keV X-ray luminosities of our sources (2.00×10^{43} erg s$^{-1} \leq L^{int}_{2-10\ keV} \leq 6.17 \times 10^{45}$ erg s^{-1}) suggest them to be luminous quasars. The N_H versus Eddington ratio diagnostic plot infers that our sample consists of a heterogeneous population that includes a small fraction (~ 12 per cent) of DOGs belonging to an early phase (Hot DOGs) during which accretion and obscuration peaks, while the remaining DOGs belong to an intermediate or late phase during which radiative feedback from the dominant AGN blows away surrounding obscuring material.

Key words: galaxies: active — quasars: general — X-rays: galaxies — galaxies: evolution — methods: observational

1 INTRODUCTION

Active Galactic Nuclei (AGN) in the local universe are known to be obscured by circumnuclear material distributed in the form of a torus (Bianchi et al. 2012; Ricci et al. 2017; Zhao et al. 2021) as envisaged by the AGN unification model (Antonucci & Miller 1985; Urry & Padovani 1995). Depending on the orientation of the obscuring torus, AGN can be broadly classified into type 1 (pole-on view) and type 2 (edge-on view). As expected, type 2 AGN exhibit higher line-of-sight column densities ($N_{H,\ LOS} \sim 10^{22} - 10^{24}$ cm^{-2} or even higher) at X-ray wavelengths (Singh et al. 2011; Ricci et al. 2015) and they constitute most of the obscured population of AGN in the local universe ($z \leq 0.05$) (Matt et al. 2000; Bianchi et al. 2012). Hard X-ray (> 10 keV) spectral studies have also revealed the presence of Compton-thick (CT) AGN with $N_{H,\ LOS} \geq 1.5 \times 10^{24}$ cm^{-2} but their fraction is likely to be small ($\sim 5-10$ per cent) among the local type 2 AGN (Comastri 2004; Burlon et al. 2011; Torres-Albà et al. 2021). Although, a much higher fraction of CT-AGN is inferred to be present at higher redshifts ($z \sim 0.5-1.5$) (Akylas et al. 2012; Ananna et al. 2019). The modelling of X-ray background

(XRB) spectrum peaking at 20−30 keV requires 10 to 40 per cent of CT-AGN (Gilli et al. 2007; Treister et al. 2009a). The local super-massive black hole (SMBH) mass function derived from the AGN luminosity function can also be reconciled with a significantly large population of CT-AGN at $z \sim 1-2$, the epoch during which AGN activity peaked (Marconi et al. 2004). Moreover, the population of obscured AGN at high−z is poorly explored and the exact fraction of CT-AGN at higher redshifts is still a subject of debate. Therefore, it is important to detect and constrain the population of obscured AGN, especially at higher redshifts.

Dust-obscured galaxies (DOGs) containing large reservoirs of gas and dust, are arguably thought to be potential hosts of obscured AGN (Narayanan et al. 2010; Suleiman et al. 2022). DOGs are defined to be bright in mid-IR but faint in optical with the flux ratio of 24 μm mid-IR band to R−band optical ($\frac{f_{24\ \mu m}}{f_R}$) ≥ 1000 (Dey et al. 2008). In general, DOGs represent the population of optically-faint high-redshift ($z \sim 1.5-2.5$) galaxies with their total 8−1000 μm IR luminosities ($10^{11} - 10^{14}\ L_\odot$) similar to local luminous IR galaxies (LIRGs) and ultra-luminous IR galaxies (ULIRGs) (Sanders & Mirabel 1996; Melbourne et al. 2012). The high IR luminosity of DOGs is explained by invoking gas-rich major merger leading to an intensely star-forming dusty merged sys-

tem (Hopkins et al. 2008; Yutani et al. 2022). The large gas reservoir is also likely to fuel as well as obscure the accreting SMBH. In fact, it is believed that the star-forming (SF) DOGs can evolve into AGN-dominated DOGs, which can eventually turn into quasars (Granato et al. 2004; Hopkins et al. 2006; Alexander & Hickox 2012). The obscured AGN are commonly detected in the extreme population of DOGs that are known as the 'Hot DOGs' characterized by hotter (up to hundreds of K) dust emission and extremely high IR luminosity ($L_{IR} \geq 10^{13}$ $L_\odot$; Tsai et al. 2015; Farrah et al. 2017). However, the presence of obscured AGN in less extreme AGN-SF composite DOGs cannot be ruled out as their spectral energy distributions (SEDs) can be well-fitted with or without AGN component (Bussmann et al. 2009; Lanzuisi et al. 2009; Teng & Veilleux 2010).

In the literature, there have been several attempts to exploit the X-ray observations of DOGs. Although, most of the previous studies have been limited either to highly luminous DOGs, *i.e.,* Hot DOGs (Stern et al. 2014; Ricci et al. 2017) or hampered with poor quality X-ray spectra (Martínez-Sansigre et al. 2007; Vito et al. 2018; Zou et al. 2020). The good quality X-ray observations of DOGs are limited only to a few relatively nearby sources (see Zappacosta et al. 2018; Assef et al. 2020; Toba et al. 2020). Considering the non-detection of X-ray emission in a large fraction of DOGs, as they fall below the detection limit of X-ray surveys, there have been attempts to examine the X-ray spectrum of the stacked emission of undetected DOGs (e.g., Fiore et al. 2008; Treister et al. 2009b). The stacked emission exhibiting flat X-ray spectrum is considered as an indication of a large fraction of CT-AGN in DOGs (Fiore et al. 2009). However, the flat X-ray spectrum can also be produced from a low-luminosity AGN having a moderate obscuration (see Georgantopoulos et al. 2008) or due to a significant population of non-AGN DOGs among the X-ray undetected DOGs (Pope et al. 2008). Therefore, deep and large-area X-ray surveys are required to examine the prevalence of obscured AGN in DOGs.

We point out that the X-ray observations from *XMM-Newton* and *Chandra* limited up to 10 keV pose a challenge to detect nearby CT-AGN as it becomes difficult to accurately determine the photoelectric absorption cut-off seen at higher energies (≥ 4.0 keV). However, for high$-z$ AGN, X-ray spectra are redshifted to lower energies, which in turn makes *XMM-Newton* and *Chandra* observations useful to determine the absorption cut-off and constrain the absorbing column density in CT-AGN (Lanzuisi et al. 2015; Koss et al. 2016). In this paper, we unveil and study the nature of AGN hosted in DOGs using deep *XMM-Newton* and *Chandra* observations available in the XMM Large-Scale Structure (XMM-LSS) field. Our study is limited within the coverage of XMM-*Spitzer* Extragalactic Representative Volume Survey (XMM-SERVS) performed in the XMM-LSS field. The choice of XMM-LSS field is based on the fact that X-ray studies of DOGs utilising deep *XMM-Newton* and *Chandra* observations have already been performed in some of the deep fields, *e.g.,* Chandra Deep Field-South (CDF-S), Chandra Deep Field-North (CDF-N), Extended Chandra Deep Field-South (ECDF-S) and Cosmic Evolution Survey (COSMOS) (see Fiore et al. 2009; Treister et al. 2009b; Georgantopoulos et al. 2011; Corral et al. 2016).

This paper is structured as follows. In Section 2, we describe our DOGs sample, selection criteria, redshifts and

multi-wavelength data. In Section 3, we provide the details of X-ray observations and data reduction. In Section 4, we discuss X-ray spectral modelling. Section 5 is devoted to the discussion on the nature and plausible evolutionary scenario of our DOGs. In Section 6, we present the conclusions of our study.

In this paper, we adopt ΛCDM cosmology with $H_0 = 70$ km s^{-1} Mpc^{-1}, $\Omega_M = 0.27$, $\Omega_\Lambda = 0.73$. Errors quoted on parameters are of 90 per cent confidence level unless stated otherwise.

2 THE SAMPLE, SELECTION CRITERIA AND REDSHIFTS

We identified 34 DOGs with sufficiently good X-ray spectral quality in the 5.3 deg^2 area of the XMM-SERVS coverage ($34°.2 \leq$ RA (J2000) $\leq 37°.125$; and $-5°.72 \leq$ DEC (J2000) $\leq -3°.87$) in the XMM-LSS field. In Table 1, we list our sample sources and other parameters, *i.e.,* source name, including RA and DEC information, 24 μm flux, $r-$band magnitude, flux ratio of 24 μm to $r-$band, redshift, and the X-ray source ID from the XMM-SERVS catalogue reported by Chen et al. (2018). In the following sub-section, we describe our method to identify DOGs and provide the details of the multi-wavelength data available in the XMM-SERVS coverage.

2.1 Identification of DOGs and multi-wavelength data in the XMM-SERVS coverage

The SERVS, a deep near-IR photometric survey, was performed with the post-cryogenic Spitzer in 3.6 μm and 4.5 μm Infrared Array Camera (IRAC) bands in the XMM-LSS region (Mauduit et al. 2012). The XMM-SERVS provides the *XMM-Newton* survey of the SERVS coverage of 5.3 deg^2 (Chen et al. 2018). The XMM-SERVS region is also covered with other multi-wavelength surveys that include UV observations from the GALEX Deep Imaging Survey[1], optical photometric observations in g, r, i, z, y, and four narrow-band filters from the Hyper Suprime-Cam Subaru Strategic Program survey (HSC-SSP; Aihara et al. 2018), Y, J, H and K_s bands photometric observations from the VISTA Deep Extragalactic Observations Survey (VIDEO; Jarvis et al. 2013), mid-IR (3.6 μm, 4.5 μm, 5.8 μm and 8.0 μm from IRAC and 24 μm, 70 μm and 160 μm from the Multi-band Imaging Photometer for *Spitzer* (MIPS)) observations from the *Spitzer* Wide-area IR Extragalactic Survey (SWIRE; Lonsdale et al. 2003); far-IR (100 μm, 160 μm from PACS and 250 μm, 350 μm and 500 μm from SPIRE) observations from the *Herschel* Multi-tiered Extragalactic Survey (HerMES; Oliver et al. 2012), and radio surveys at various frequencies (see Singh et al. 2014; Heywood et al. 2020).

To identify DOGs in the XMM-SERVS region, we utilised 24 μm SWIRE and wide HSC-SSP optical data and followed the method described in Kayal et al. (2022). We began with the 24 μm source catalogue (signal-to-noise ratio (SNR) $\geq$

---

[1] http://www.galex.caltech.edu/researcher/techdoc-ch2.html

Table 1. The sample of X-ray detected DOGs in the XMM-SERVS coverage of the XMM-LSS field

Source Name	$S_{24\ \mu m}$ (mJy)	m_r (mag)	$S_{24\ \mu m}/S_r$	Redshift	Ref.	XID
(1)	(2)	(3)	(4)	(5)	(6)	(7)
J02:16:57-04:02:02	0.806±0.026	24.96±0.10	2141.7	$1.155^{+0.146}_{-0.122}$	D23	XMM00059
J02:17:05-04:56:54	0.601±0.023	25.64±0.03	3005.0	$1.732^{+0.284}_{-0.098}$	N23	XMM00131
J02:17:06-05:25:47	0.648±0.022	24.53±0.02	1159.3	$1.843^{+0.121}_{-1.143}$	N23	XMM00136
J02:17:15-04:01:17	0.708±0.028	25.12±0.09	2187.2	$2.188^{+0.401}_{-1.822}$	D23	XMM00191
J02:17:16-04:30:09	0.923±0.027	24.06±0.01	1074.4	0.5862 ± 0.0079 (s)	PR	XMM00205
J02:17:22-04:36:55	1.282±0.024	25.71±0.06	6788.8	$4.648^{+0.091}_{-0.251}$	N23	XMM00250
J02:17:24-04:18:44	0.412±0.027	25.94±0.05	2706.8	$2.948^{+0.080}_{-1.000}$	N23	XMM00267
J02:17:33-04:06:13	0.436±0.026	24.85±0.03	1045.5	$1.287^{+0.033}_{-0.033}$	D23	XMM00359
J02:17:36-04:59:11	0.391±0.026	25.80±0.04	2255.6	$3.067^{+0.165}_{-0.547}$	N23	XMM00393
J02:17:36-05:01:07	0.544±0.027	24.71±0.02	1144.4	1.4210 ± 0.0182 (s)	UDSz	XMM00395
J02:17:40-04:32:43	0.391±0.024	24.99±0.02	1071.9	$1.732^{+0.338}_{-0.108}$	N23	XMM00421
J02:17:49-05:23:07	8.104±0.024	22.63±0.01	2534.3	0.8420 ± 0.0092 (s)	PR	XMM00497
J02:18:37-04:29:50	0.579±0.027	24.68±0.01	1193.1	$1.473^{+0.115}_{-0.345}$	N23	XMM00860
J02:19:01-04:24:41	0.438±0.023	25.40±0.03	1756.8	$1.759^{+0.241}_{-0.091}$	N23	XMM01034
J02:19:31-04:49:41	1.040±0.027	24.29±0.01	1501.2	0.7953 ± 0.0089 (s)	PR	XMM01279
J02:19:56-05:05:01	1.217±0.024	25.06±0.02	3548.3	$1.652^{+3.768}_{-0.0269}$	N23	XMM01464
J02:20:32-04:50:02	4.436±0.040	22.68±0.01	1454.4	1.084 ± 0.0011 (s)	VI	XMM01723
J02:20:33-05:08:55	1.346±0.028	24.20±0.01	1775.1	$2.048^{+0.383}_{-0.076}$	N23	XMM01731
J02:20:34-05:06:58	0.833±0.022	24.74±0.01	1808.1	$2.870^{+0.136}_{-0.258}$	N23	XMM01740
J02:21:30-04:02:03	1.013±0.022	25.84±0.10	6070.7	$1.096^{+0.387}_{-0.335}$	D23	XMM02186
J02:21:50-05:23:58	0.647±0.024	24.45±0.02	1077.9	$1.900^{+0.153}_{-0.166}$	N23	XMM02347
J02:22:32-04:49:09	0.682±0.021	24.39±0.02	1080.9	$1.815^{+1.106}_{-0.099}$	N23	XMM02660
J02:23:30-04:34:42	0.668±0.022	24.47±0.02	1132.8	$2.300^{+0.319}_{-0.289}$	N23	XMM03098
J02:23:38-04:05:13	1.684±0.027	24.39±0.04	2660.3	$3.275^{+0.292}_{-0.162}$	N23	XMM03153
J02:24:01-04:05:28	0.919±0.029	25.41±0.08	3687.1	$1.678^{+0.148}_{-0.053}$	N23	XMM03342
J02:24:59-04:14:14	3.239±0.029	22.71±0.01	1092.0	$1.900^{+1.025}_{-0.118}$	N23	XMM03798
J02:25:12-04:19:11	0.805±0.025	24.16±0.01	1031.1	$1.759^{+0.065}_{-0.141}$	N23	XMM03900
J02:25:14-04:34:21	2.376±0.040	23.09±0.01	1131.5	$3.538^{+0.069}_{-0.212}$	N23	XMM03916
J02:26:06-04:44:19	1.259±0.028	24.62±0.03	2460.1	$1.732^{+0.295}_{-0.082}$	N23	XMM04259
J02:26:24-04:13:43	0.647±0.027	25.10±0.04	1957.8	$1.652^{+0.075}_{-0.074}$	N23	XMM04404
J02:26:33-04:43:07	0.756±0.024	24.42±0.03	1228.2	$2.333^{+0.748}_{-0.557}$	N23	XMM04475
J02:26:47-05:31:13	1.112±0.025	24.67±0.15	2256.0	$1.070^{+0.231}_{-0.185}$	D23	XMM04583
J02:27:16-04:32:42	0.887±0.028	24.59±0.01	1683.1	$1.759^{+0.325}_{-0.055}$	N23	XMM04804
J02:27:29-04:48:58	0.620±0.027	25.08±0.04	1854.3	$1.652^{+0.123}_{-0.078}$	N23	XMM04899

Notes - Column (1): Source name based on its RA (J2000) and DEC (J2000), Column (2): 24 μm flux from the SWIRE survey, Column (3): $r-$band magnitude from the HSC-SSP catalogue, Column (4): flux ratio of 24 μm band to $r-$band, Column (5): Redshift, all are photo$-z$ except those marked with '(s)' for spectroscopic redshift, Column (6): Reference for the redshift (N23 - Nyland et al. (2023); D23 - Desprez et al. (2023), PR - PRIsm MUlti-Object Survey (PRIMUS), VI - VIMOS Public Extragalactic Redshift Survey (VIPERS) and UDSz - UKIDSS Ultra-Deep Survey, Column (7): X-ray source ID from the XMM-SERVS catalogue reported by Chen et al. (2018).

5) and identified their optical counterparts. Since the positional uncertainty of 24 μm sources ($2''.0$) is relatively larger than that of the optical sources ($0''.2$), we used positions of 3.6 μm IRAC counterparts of 24 μm sources from the SWIRE band-merged catalogue[2] to increase the reliability of the positional cross-matching. The optical and band-merged 3.6 μm $-$ 24 μm source catalogues were cross-matched using a radius of $1''.0$ and the nearest match was considered as a true counterpart. We found optical as well as 3.6 μm counterparts for all our 24 μm sources, owing to a much higher sensitivity in the optical (5σ limiting magnitude in $i-$band (m_i) 26.2) and

3.6 μm band (7.3 μJy beam^{-1} at 5σ) than that of the 24 μm band (0.45 mJy beam^{-1} at 5σ).

To select DOGs, we used the conventional criterion of flux ratio of 24 μm to $r-$band optical ($\frac{f_{24\ \mu m}}{f_r}$) $\geq$ 1000, which corresponds to the colour cut of $r - [24] \geq 7.5$, where magnitudes are in the AB system (see Dey et al. 2008; Fiore et al. 2008; Toba et al. 2015). Using the aforementioned criterion, we found a total of 1239 DOGs within 5.3 deg^2 of the XMM-SERVS region. To study the X-ray properties of DOGs, we searched for their X-ray counterparts using the XMM-SERVS X-ray point source catalogue. The availability of the optical$-$NIR$-$X-ray band-merged catalogue from Chen et al. (2018), which contains optical (from CFHTLS and HSC-SSP) and near-IR counterparts (from VIDEO and SERVS) of X-ray point sources, allows us to identify the X-

ray counterparts of the DOGs by simply cross-matching the optical positions of it with our optical-3.6 μm-24 μm band-merged catalogue using a tolerance radius of $1''.0$. This exercise gives us only 89/1239 (7.2 per cent) DOGs with X-ray counterparts. The fraction of X-ray detected DOGs is similar to that reported in our previous study (Kayal et al. 2022) that used data of similar sensitivities.

We note that, for 89 DOGs, the total X-ray counts in $0.5-10$ keV full band ranges from 44 to 1038 with a median value of 124. The total count value listed in the XMM-SERVS catalogue represents the sum of the counts from all the three imaging detectors (PN, MOS1 and MOS2) in the *XMM-Newton* observations. The total X-ray counts of a source determines its X-ray spectral quality. Therefore, to obtain reasonably good-quality X-ray spectra, we restricted our sample to 34/89 sources with total counts ≥ 150 in $0.5-10$ keV energy band or those having additional *Chandra* observations. We note that the cut-off limit on the total counts is based on our qualitative assessment of spectral quality. It ensures that our X-ray spectra are better than those used in several previous studies (e.g., Martínez-Sansigre et al. 2007; Vito et al. 2018; Zou et al. 2020; Glikman et al. 2024) which reported X-ray spectra of DOGs with ≤ 50 total counts in $0.5-10$ keV energy band. The better spectral quality allows us to obtain reliable constraints on the continuum spectral shape and absorption column density. We would like to point out that the total X-ray counts found in our analysis may differ from the value listed in the XMM-SERVS catalogue, as we have added more recent data, whenever available, and excluded observations in which source$-$of$-$interest falls within CCD gaps or in the peripheral region (see Section 3).

Further, our final sample of 34 sources represents a faint population of DOGs having 24 μm flux ($S_{24 \mu m}$) in the range of 0.39 mJy to 8.11 mJy with a median value of 0.81 mJy. As expected, our DOGs are also faint in the optical wavelengths with m_r distributed across 22.64 to 25.94, with a median value of 24.68. The faintness of DOGs can be attributed to their high redshifts ($0.59 \leq z \leq 4.65$, $z_{\mathrm{median}} = 1.75$). Therefore, unlike some of the previous studies limited to relatively bright DOGs (e.g., Lanzuisi et al. 2009; Zou et al. 2020), our sample allows us to probe a fainter population of DOGs residing at higher redshifts.

2.2 Spectroscopic and photometric redshifts of DOGs

Redshift estimates of DOGs are essential for their X-ray spectral fittings and luminosity measurements. To obtain the redshifts of our DOGs, we utilised various redshift measurement campaigns performed in the XMM-SERVS region. For instance, we used the spectroscopic redshift catalogue from the HSC-SSP PDR-3 that includes spectroscopic redshifts from different campaigns, *i.e.,* PRIsm MUlti-Object Survey (PRIMUS; Coil et al. 2011), VIMOS Public Extragalactic Redshift Survey (VIPERS; Garilli et al. 2014), VIMOS VLT Deep Survey (VVDS; Le Fèvre et al. 2013), SDSS Baryon Oscillation Spectroscopic Survey (SDSS-BOSS) programme (Dawson et al. 2013; Menzel et al. 2016). We have also used Chen et al. (2018) catalogue that lists spectroscopic redshifts for X-ray sources, whenever available. They used UKIDSS Ultra-Deep Survey (UDSz; Bradshaw et al. 2013; McLure et al. 2013), 3D-HST Survey (Skelton et al. 2014; Momcheva et al. 2016) and other publicly available spectroscopic redshift

catalogues[3]. From these spec$-z$ catalogues, we find spectroscopic redshifts for only 05 of our 34 X-ray detected DOGs (see Table 1).

For the remaining 29 sources, we obtained photometric redshifts using multi-band photometry-based photo$-z$ catalogues reported by Nyland et al. (2023) and Desprez et al. (2023). We note that several photo$-z$ campaigns are available in the XMM-SERVS region, *e.g.,* CFHTLS-based photo$-z$ estimates (Ilbert et al. 2006; Coupon et al. 2009), HSC-SSP-based photo$-z$ estimates (Tanaka et al. 2018; Schuldt et al. 2021). We prefer to use more accurate photo$-z$ estimates derived from the multi-band photometry spanning across optical to near-IR. Nyland et al. (2023) estimated photometric redshifts using the Tractor image-modelling software-based de-blended multi-band forced photometry across 13 optical to near-IR bands (u' band from the CFHTLS, g, r, i, z and y bands from the HSC-SSP, Z, Y, J, H, and Ks bands from the VIDEO and 3.6 μm and 4.5 μm bands from the *Spitzer*/DeepDrill). The photo$-z$ estimates based on the forced photometry are more accurate and supersede previous estimates based on the traditional position-matched multi-band photometry (e.g., Chen et al. 2018; Ni et al. 2021; Zou et al. 2021, 2022). Previous test$-$bed study on the Tractor-based photo$-z$ estimate limited to 1.0 deg^2 in the XMM-SERVS, showed accurate photometric redshifts with normalized median absolute deviation (NMAD), $\sigma_{\mathrm{NMAD}} \leq 0.08$ and an outlier fraction of only ≤ 1.5 per cent (see Nyland et al. 2017).

We note that the photo$-z$ estimates reported in Nyland et al. (2023) are limited only to the VIDEO/*Spitzer* Deep-Drill region of 4.5 deg^2, which does not fully cover the XMM-SERVS field of 5.3 deg^2. We find that only 24/29 of our DOGs falling within the VIDEO region have photo$-z$ estimates from Nyland et al. (2023). For the remaining 05/29 DOGs, we considered photo$-z$ estimates from Desprez et al. (2023), who used multi$-$band photometric data (u, $u^{\star}$ from the CFHT-MegaCam, g, r, i, z, and y from the HSC-SSP, and Y, J, H, and K_s data from the VIDEO, whenever available). The photo$-z$ for sources falling outside the VIDEO region are based on only seven-band optical data. The photo$-z$ estimates are precise with $\sigma_{\mathrm{NMAD}} \leq 0.04$ down to $m_i = 25$, and an outlier fraction of ≤ 6 per cent. Further, we point out that Desprez et al. (2023) reported two different versions of the photo$-z$ catalogues, *i.e.,* one version used the HSC pipeline for the photometric extraction and Phosphoros code for the redshift estimation, while the second version used Source Extractor for the photometry and Le PHARE code (Arnouts et al. 1999; Ilbert et al. 2006) for the redshift measurements. We used the second version of the photo$-z$ catalogue due to its slightly better performance. We found photo$-z$ for all remaining 05 sources from Desprez et al. (2023) photo$-z$ catalogue. Thus, in total, we found redshift estimates for all 34 DOGs, *i.e.,* spec$-z$ for 05 sources and photo$-z$ for 29 sources (see Table 1).

---

[3] https://www.nottingham.ac.uk/astronomy/UDS/data/data.html

3 X-RAY OBSERVATIONS AND DATA REDUCTION

To study the X-ray spectral properties of our DOGs, we used archival *XMM-Newton* observations, which were performed mainly under the XMM-SERVS project. Using a total of 155 pointings, XMM-SERVS observations provide a nearly uniform coverage of 5.3 deg^2 sky-area in the XMM-LSS field (Chen et al. 2018). The XMM-SERVS project used a total of 2.7 Ms of flare-filtered exposure time, which includes 1.3 Ms observations carried out in AO-15 and all the available archival *XMM-Newton* data from other surveys, *e.g.,* XMM-LSS survey (Pacaud et al. 2006; Pierre et al. 2016), *XMM-Newton* Medium Deep Survey (XMDS, Chiappetti et al. 2005), Subaru *XMM-Newton* Deep Survey (SXDS, Ueda et al. 2008) and XMM-XXL-North field (Pierre et al. 2016). The combination of different epochs of archival data makes XMM-SERVS survey the deepest X-ray survey in the XMM-LSS field. The depth of the XMM-SERVS survey is comparable to some of the deep small−area surveys, such as SXDS covering only 1.14 deg^2 (Ueda et al. 2008) and XMM-COSMOS covering only 2.0 deg^2 (Cappelluti et al. 2009).

For each of our sample sources, we downloaded all the available X-ray data from the *XMM-Newton* Science Archive[4]. In order to improve the X-ray spectral quality, we also checked the availability of *Chandra* observations of our sample sources using *Chandra* Source Catalog Release 2.0 (CSA 2.0[5]). Three of our sample sources have *Chandra* archival data with total counts > 10. In Table A1, we provide the details of X-ray observations, *i.e.,* observation ID, observation date, observation time and X-ray source ID from the XMM-SERVS catalogue. To gain further improvement in the X-ray spectral quality of our faint sources, we added all the available *XMM-Newton* data, for a given source, taken at different epochs. We caution that the addition of multi-epoch data renders average spectral properties, if a source is variable across different epochs.

3.1 *XMM-Newton* data reduction

We reduced the *XMM-Newton* pn and MOS data using Science Analysis System (SAS) v21.0.0. The Observation Data Files (ODFs) were processed using EPICPROC tasks (EPPROC and EMPROC tasks for pn and MOS, respectively) to create pn, MOS1, and MOS2, event files for each observation ID. From each event file, we created good time interval (GTI) event file using the EVSELECT task. The flaring background time intervals were identified from the single-event light curves of high (10−12 keV) and low (0.3−10 keV) energies and the time intervals exceeding count rates 3σ above the mean value were removed. The GTI files were calibrated using the most recent calibration files. Further, we filtered the event files at the energy ranges that overlap with the instrumental background lines, *i.e.,* Cu lines at 7.2−7.6 and 7.8−8.2 keV for pn.

For each observation ID, we extracted the spectrum from each detector using a circular region centred on the source position. The radius of the source extraction region is in the range of 15″ to 25″ depending on the offset of the target

source from the on-axis. The background spectrum was extracted from a neighbouring source-free region using a circular aperture of 40″ radius (see Figure A1). We note that despite moderately deep XMM-SERVS observations, our DOGs tend to suffer from poor photon statistics. Therefore, for a source with multi-epoch observations, we added the source spectra from individual observation IDs. The background spectra from individual observation IDs were also added. To increase the spectral quality further, we combined the spectra from pn, MOS1 and MOS2 using EPICSPECCOMBINE task (see Figure A2 and Figure A3). To combine the spectra from all three detectors, we ensured a common energy range of 0.5−10 keV. The response and auxiliary files were computed by averaging the individual files of each detector.

3.2 *Chandra* data reduction

We reduced *Chandra*/ACIS data using Chandra Interactive Analysis of Observations (CIAO) software version 4.15 (CALDB version 4.10.4). For data reduction, we followed the standard procedure, which includes the removal of hot pixels, cosmic afterglows and background flaring time intervals. The cleaned event files were calibrated using the most recent calibration files. From each individual observation, we have extracted the source spectrum using the SPECEXTRACT task and considered a circular extraction region centred on the X-ray source. The radius of extraction region includes 90 per cent Encircled Energy Fraction (EEF) and is around 1″.0 − 3″.0 depending on the off-axis angle. The background spectrum was extracted from a source-free circular region of 12″.0 − 15″.0 radius selected in the same CCD chip. The SPECEXTRACT task also generates auxiliary and response matrix files. In case of sources having multiple *Chandra*/ACIS observations, we added all individual spectra of a source. We created combined source spectrum, background spectrum, response, and auxiliary matrices using the COMBINE_SPECTRA task in the CIAO.

4 X-RAY SPECTRAL ANALYSIS

We performed X-ray spectral fittings of our sample sources using XSPEC v12.13.0c (Arnaud 1996). In order to get reliable goodness-of-fit statistics with moderate to low-count spectra, we preferred to use Cash statistics (Cash 1979) instead of χ^2 statistics. We attempted to fit the X-ray spectra of our sample sources using a simple absorbed power law model as well as with a physically motivated model.

4.1 X-ray spectral fitting with a simple absorbed power law

To fit the X-ray spectra, we began with a baseline model characterised by a simple absorbed power law, which can be expressed as TBABS × (ZTBABS × POWERLAW). The first absorption component (TBABS) accounts for the Galactic absorption column density ($N_{\rm H, \, Gal}$), which is fixed to the value obtained from the NASA's HEASARC $N_{\rm H}$ calculator[6]. The galactic absorption in the direction of the XMM-LSS field

---

[4] https://nxsa.esac.esa.int/nxsa-web/search
[5] https://cxc.cfa.harvard.edu/csc/

[6] https://heasarc.gsfc.nasa.gov/cgi-bin/Tools/w3nh/w3nh.pl

is found to be in the range of 1.86×10^{20} cm^{-2} $-$ 2.45×10^{20} cm^{-2}. The second absorption component accounts for the photoelectric absorption at the source redshift. To constrain the absorbing column density accurately, we kept the power law photon index (Γ) as a free parameter. However, we caution that $0.5-10$ keV X-ray spectra of heavily obscured AGN can also be mimicked with a flat power law absorbed with a low column density (George & Fabian 1991; Georgantopoulos et al. 2011). Therefore, to avoid the degeneracy between photon index (Γ) and $N_{\rm H}$, and to place reliable constraints on $N_{\rm H}$, we fixed Γ to 2.0, whenever spectral fitting rendered a flat ($\Gamma < 1.7$) photon index. Considering the fact that AGN generally exhibit a steep photon index in the range of 1.8 to 2.1, it is a common practice to fix the photon index to a typical value ($1.8-2.1$) when dealing with low-count X-ray spectra (see Tozzi et al. 2006; Corral et al. 2016; Zou et al. 2020). We note that the fit statistics do not show any appreciable change if the photon index is altered from 2.0 to 1.9 or 1.8. The best-fitted spectral parameters obtained from the absorbed power law model are listed in Table 2. To our baseline model (simple absorbed power law), we attempted to add a reflection component using PEXRAV, a phenomenological model, which considers reflection from a semi-infinite slab of neutral medium (Magdziarz & Zdziarski 1995). However, we found either no or insignificant improvement in the fit statistics. Thus, a simple absorbed power law seems adequate for fitting the X-ray spectra of the most of our sample sources.

In one of our sample sources (XMM01723), residuals seen at the soft energies (< 2.0 keV) can be accounted for with an additional power law which is interpreted as the scattered AGN emission reaching directly to the observer without piercing through the obscuring material. The photon index of the scattered power law is tied with that of the transmitted power law component. The addition of a scattered power law improves the fit statistics from Cstat/d.o.f. = 206.2/172 (1.20) to 200.5/171 (1.17). In XMM01723, the ratio of normalizations of the scattered power law component to the direct power law component is found to be only 0.07, which shows that the leaked scattered emission is much weaker than the directly transmitted component, as expected in case of heavily obscured sources. We note that the presence of the scattered power law component in XMM01723 is consistent with the previous X-ray studies of DOGs and dust-reddened quasar samples (e.g., Corral et al. 2016; LaMassa et al. 2016; Glikman et al. 2017).

The Fe Kα emission line, a ubiquitous feature in nearby AGN spectra, is detected in five of our sample sources (see Table 2). The presence of the Fe Kα emission line is apparent from the residuals. The addition of a line component yields an improvement in the fit statistics. For instance, in the case of XMM03916, the addition of a line component representing Fe Kα line emission improves the fit statistics from Cstat/d.o.f. = 176.75/167 (1.06) to Cstat/d.o.f. = 171.49/165 (1.04). The Fe Kα line is fitted with a narrow unresolved (<100 eV) Gaussian by fixing the line-width to 1 eV and keeping the line energy as a free parameter. In all five sources, the energy of the emission line in the rest-frame corresponds to 6.4 keV, *i.e.,* the energy of the neutral Fe Kα line. The detection of the Fe Kα line also provides confirmation of redshift accuracy. We note that the detection of the Fe Kα emission line in the re-

maining sample sources might be hindered due to low counts in their spectra.

The equivalent widths (EWs) of Fe Kα lines in our sample sources are found to be in the range of 0.06 keV to 0.26 keV. We point out that, in general, heavily obscured AGN show high EWs (≥ 0.5 keV) of Fe Kα emission line (Maiolino et al. 1998; Matt et al. 2000; Singh et al. 2011). However, in our sample, heavily obscured sources (XMM00497, XMM01723 and XMM03916) show low EWs, which can be explained from the well-known Baldwin effect, also known as Iwasawa–Taniguchi effect (Baldwin 1977; Iwasawa & Taniguchi 1993), an anti-correlation between EW of Fe Kα line and X-ray luminosity (see Boorman et al. 2018; Matt & Iwasawa 2019). The heavily obscured sources in our sample have high X-ray luminosities ($L^{\rm int}_{2.0-10 \rm \ keV} \sim 10^{44} - 10^{45}$ erg s^{-1}) which can give rise to systematically lower EWs of Fe Kα lines. In fact, several CT-AGN of high X-ray luminosities ($\geq 10^{44}$ erg s^{-1}) are known to exhibit moderate EWs of a few hundred eVs or lower (see Fukazawa et al. 2011; Iwasawa et al. 2012; Boorman et al. 2018). Although, we note that the Fe Kα line EW estimates of our sample DOGs ought to be treated with caution due to their low-count spectra.

4.2 X-ray spectral fitting with BORUS02 model

In addition to modelling the X-ray spectra of our sample sources with a simple absorbed power law, we also attempted to use a physically motivated model which considers reprocessing of X-ray emission from the circumnuclear material in AGN. It is widely accepted that the circumnuclear material in AGN is distributed in the form of a torus (Elitzur 2006; Netzer 2015; Zhao et al. 2021). The torus-based models have commonly been used to model the X-ray spectra of DOGs, even those with low counts in their spectra (see Vito et al. 2018; Laloux et al. 2023; Yan et al. 2023). Therefore, we used BORUS02 (Baloković et al. 2018), a torus-based model, which assumes a smooth distribution of matter in a spherical geometry with two polar conical cuts. This model also accounts for Compton scattering of X-ray photons and Fe K emission lines in a self-consistent manner.

To fit the X-ray spectra of our DOGs, we used a model that can be expressed as $c_1 \times$ TBABS $\times$ (BORUS02 + ZTBABS $\times$ CABS $\times$ CUTOFFPL), where c_1 represents cross-calibration factor in case of fitting multi-instrument spectra. The transmitted component is represented by a cut-off power law (CUTOFFPL) which includes the effects of absorption (ZTBABS) and Compton-scattering losses along the line-of-sight (CABS). The BORUS02 model accounts for the reprocessed AGN emission component. We used the BORUS02 model in its standard form by keeping all the parameters free. Although, we tied line-of-sight column density to the average torus column density considering low-count spectra. Often, we were unable to constrain the covering factor (f_c) and we fixed it to 0.5, whenever it remained unconstrained. In case of unusually flat (< 1.7) photon index, we fixed it to the value obtained from the absorbed power law model, if constrained, otherwise, we fixed it to 2.0.

We note that the BORUS02 model inherently includes reflection component, and, for the most of our sample sources, the reflection component is insignificant in comparison to the transmitted component (see Figure A4). Due to a very weak or nearly absent reflection component, the BORUS02 model is

Table 2. The best-fitted spectral parameters using absorbed power law model

XID	Model	N_{H} $(10^{22}\ \mathrm{cm}^{-2})$	Γ	Γ_{norm} (10^{-5})	$\mathrm{pl}^{\mathrm{sct}}_{\mathrm{norm}}$ (10^{-5})	E_{Fe} (keV)	EW_{Fe} (keV)	Cstat (dof)	P_{CT}
(1)	(2)	(3)	(4)	(5)	(6)	(7)	(8)	(9)	(10)
XMM00059	abs*pl+L	$1.77^{+0.50}_{-0.33}$	2.0^{f}	$1.74^{+0.23}_{-0.16}$		$2.94^{+0.05}_{-0.60}$	$0.18^{+0.14}_{-0.16}$	596.8 (656)	0.0
XMM00131	abs*pl	$1.94^{+0.85}_{-0.60}$	2.0^{f}	$0.91^{+0.14}_{-0.11}$				531.9 (530)	0.0
XMM00136	abs*pl	$1.83^{+1.36}_{-0.85}$	2.0^{f}	$0.38^{+0.09}_{-0.07}$				174.9 (209)	0.0
XMM00191	abs*pl	$44.22^{+12.16}_{-8.86}$	2.0^{f}	$3.19^{+0.74}_{-0.55}$				490.0 (490)	0.0
XMM00205	abs*pl	$2.94^{+1.56}_{-0.82}$	2.0^{f}	$0.61^{+0.20}_{-0.12}$				185.2 (189)	0.0
XMM00250	abs*pl	$31.66^{+56.51}_{-11.18}$	$2.15^{+1.25}_{-0.32}$	$0.53^{+1.70}_{-0.15}$				218.7 (216)	0.0
XMM00267	abs*pl+L	$3.29^{+1.97}_{-1.33}$	$1.72^{+0.23}_{-0.17}$	$1.15^{+0.27}_{-0.17}$		$1.49^{+0.32}_{-0.43}$	$0.06^{+0.04}_{-0.06}$	655.3 (696)	0.0
XMM00359	abs*pl	$1.43^{+0.41}_{-0.41}$	$2.52^{+0.06}_{-0.44}$	$0.36^{+0.11}_{-0.05}$				252.4 (292)	0.0
XMM00393	abs*pl	$9.72^{+11.73}_{-3.91}$	$2.14^{+0.43}_{-0.36}$	$0.40^{+0.32}_{-0.12}$				234.4 (228)	0.0
XMM00395	abs*pl	$1.10^{+0.66}_{-0.46}$	2.0^{f}	$0.35^{+0.07}_{-0.05}$				333.5 (369)	0.0
XMM00421	abs*pl	$0.49^{+0.74}_{-0.38}$	2.0^{f}	$0.40^{+0.09}_{-0.06}$				281.2 (312)	0.0
XMM00497	abs*pl+L	$13.12^{+2.29}_{-1.53}$	2.0^{f}	$5.58^{+0.82}_{-0.58}$		$3.19^{+0.05}_{-0.05}$	$0.17^{+0.09}_{-0.10}$	637.6 (656)	0.0
XMM00860	abs*pl	$3.37^{+2.74}_{-1.42}$	$2.04^{+0.51}_{-0.43}$	$0.36^{+0.26}_{-0.12}$				226.8 (233)	0.0
XMM01034	abs*pl	$1.40^{+1.42}_{-0.83}$	2.0^{f}	$0.25^{+0.07}_{-0.05}$				225.0 (232)	0.0
XMM01279	abs*pl	$1.17^{+0.36}_{-0.25}$	2.0^{f}	$1.29^{+0.19}_{-0.15}$				500.9 (616)	0.0
XMM01464	abs*pl	$0.86^{+0.87}_{-0.56}$	$1.91^{+0.28}_{-0.20}$	$0.45^{+0.12}_{-0.07}$				412.3 (479)	0.0
XMM01723	abs*pl+pl+L	$18.62^{+88.91}_{-5.26}$	2.0^{f}	$0.83^{+2.33}_{-0.22}$	$0.06^{+0.06}_{-0.02}$	$3.09^{+0.40}_{-0.05}$	$0.14^{+0.63}_{-0.12}$	200.5 (171)	0.01
XMM01731	abs*pl	$7.03^{+8.10}_{-2.89}$	$2.42^{+1.75}_{-0.63}$	$0.75^{+1.61}_{-0.30}$				239.3 (238)	0.0
XMM01740	abs*pl	$6.17^{+18.97}_{-3.30}$	2.0^{f}	$0.19^{+0.19}_{-0.06}$				110.0 (127)	0.0
XMM02186	abs*pl	$0.89^{+0.85}_{-0.44}$	2.0^{f}	$0.54^{+0.18}_{-0.12}$				115.1 (155)	0.0
XMM02347	abs*pl	$3.97^{+2.53}_{-1.31}$	2.0^{f}	$0.37^{+0.11}_{-0.07}$				265.2 (264)	0.0
XMM02660	abs*pl	$5.62^{+4.42}_{-1.76}$	$1.89^{+0.70}_{-0.31}$	$0.79^{+0.75}_{-0.21}$				245.3 (287)	0.0
XMM03098	abs*pl	$0.92^{+2.04}_{-0.71}$	2.0^{f}	$0.28^{+0.09}_{-0.04}$				210.0 (238)	0.0
XMM03153	abs*pl	$2.31^{+3.60}_{-1.70}$	$1.76^{+0.36}_{-0.20}$	$0.37^{+0.13}_{-0.06}$				356.8 (376)	0.0
XMM03342	abs*pl	$1.18^{+4.13}_{-0.77}$	$2.22^{+0.74}_{-0.43}$	$0.21^{+0.28}_{-0.06}$				141.1 (130)	0.0
XMM03798	abs*pl	$4.86^{+3.34}_{-1.66}$	$2.32^{+0.60}_{-0.39}$	$0.67^{+0.46}_{-0.19}$				221.7 (248)	0.0
XMM03900	abs*pl	$5.49^{+1.52}_{-1.14}$	2.0^{f}	$1.64^{+0.24}_{-0.19}$				572.0 (637)	0.0
XMM03916	abs*pl+L	$114.84^{+49.89}_{-28.94}$	2.0^{f}	$0.97^{+0.42}_{-0.24}$		$1.49^{+0.22}_{-0.17}$	$0.26^{+0.60}_{-0.22}$	171.5 (166)	0.12
XMM04259	abs*pl	$13.79^{+16.32}_{-5.31}$	$1.79^{+1.04}_{-0.47}$	$0.49^{+1.15}_{-0.23}$				192.0 (212)	0.0
XMM04404	abs*pl	$1.55^{+0.53}_{-0.53}$	$1.87^{+0.68}_{-0.29}$	$0.54^{+0.17}_{-0.07}$				327.4 (387)	0.0
XMM04475	abs*pl	$0.79^{+8.99}_{-0.48}$	2.0^{f}	$0.12^{+0.10}_{-0.02}$				308.0 (305)	0.0
XMM04583	abs*pl	$3.49^{+1.26}_{-0.82}$	2.0^{f}	$1.08^{+0.25}_{-0.19}$				412.3 (462)	0.0
XMM04804	abs*pl	$3.86^{+3.17}_{-1.64}$	$2.07^{+0.56}_{-0.39}$	$0.50^{+0.35}_{-0.15}$				224.8 (234)	0.0
XMM04899	abs*pl	$9.00^{+3.71}_{-2.24}$	2.0^{f}	$0.75^{+0.18}_{-0.12}$				295.3 (328)	0.0

Notes: Column (1): Source XIDs, Column (2): the best-fit model where 'abs' denotes absorption component, 'pl' denotes power law, 'L' denotes emission line and an additional 'pl' denotes the scattered power law, Column (3): line-of-sight column density, Column (4): photon index, Column(5): power law normalisation, Column (6): normalisation of the scattered power law component, Column (7): Fe Kα line energy in the observed−frame, Column (8): equivalent width of Fe Kα line, Column (9): Cash statistics and degrees of freedom of the spectral fit, Column (10): MCMC-based probability of source being a CT-AGN.

unable to reproduce the Fe Kα line self-consistently. Therefore, we added the Fe Kα emission line in five of our sample sources in which the presence of the emission line was evident from the absorbed power law model fittings. We kept the line width fixed to 1 eV and the line energy as a free parameter. The Fe Kα line parameters (line energy and EW) are similar to those found in the absorbed power law model fittings. In XMM01723, an additional cutoff power law representing a leaked or scattered component of intrinsic emission marginally improves the fit-statistics, which is consistent with the spectral fitting performed with the absorbed power law model (see Section 4.1). In Table 3, we list the best-fitted

parameters provided by the borus02. In Figure A4, we show the best-fitted spectra of our sample sources modelled with the borus02 model. Based on the comparison of fit statistics listed in Table 2 and Table 3, we find that both simple absorbed power law as well as borus02 model provide reasonably good fits to the X-ray spectra of our sample sources.

Table 3. The best-fitted spectral parameters using BORUS02 model

XID	Model	$N_{\rm H}$ $(10^{22}\,{\rm cm}^{-2})$	Γ	$\Gamma_{\rm norm}$ (10^{-5})	$\mathrm{pl}_{\rm norm}^{\rm sct}$ (10^{-5})	$E_{\rm Fe}$ (keV)	$EW_{\rm Fe}$ (keV)	Cstat (dof)	$P_{\rm CT}$
(1)	(2)	(3)	(4)	(5)	(6)	(7)	(8)	(9)	(10)
XMM00059	B02+L	$1.81^{+0.45}_{-0.37}$	2.0^f	$1.81^{+0.23}_{-0.19}$		$2.94^{+0.05}_{-0.49}$	$0.18^{+0.15}_{-0.16}$	597.9 (656)	0.0
XMM00131	B02	$1.99^{+0.73}_{-0.70}$	2.0^f	$0.95^{+0.13}_{-0.13}$				532.6 (530)	0.0
XMM00136	B02	$1.89^{+1.14}_{-0.77}$	2.0^f	$0.39^{+0.09}_{-0.07}$				175.5 (209)	0.0
XMM00191	B02	$45.00^{+13.97}_{-8.50}$	2.0^f	$4.63^{+1.75}_{-0.96}$				490.3 (490)	0.0
XMM00205	B02	$2.87^{+1.54}_{-0.85}$	2.0^f	$0.62^{+0.22}_{-0.14}$				185.4 (189)	0.0
XMM00250	B02	$31.00^{+23.32}_{-18.79}$	$2.12^{+0.43}_{-0.49}$	$0.66^{+0.73}_{-0.34}$				218.7 (216)	0.0
XMM00267	B02+L	$3.21^{+1.73}_{-1.53}$	$1.69^{+0.22}_{-0.18}$	$1.18^{+0.26}_{-0.19}$		$1.49^{+0.38}_{-0.06}$	$0.06^{+0.04}_{-0.06}$	655.6 (696)	0.0
XMM00359	B02	$1.24^{+0.29}_{-0.24}$	$2.51^{+0.07}_{-0.40}$	$0.37^{+0.09}_{-0.05}$				252.5 (291)	0.0
XMM00393	B02	$9.57^{+9.94}_{-5.60}$	$2.10^{+0.44}_{-0.47}$	$0.43^{+0.35}_{-0.17}$				234.3 (228)	0.0
XMM00395	B02	$1.63^{+0.15}_{-0.60}$	2.0^f	$0.37^{+0.07}_{-0.04}$				337.6 (369)	0.0
XMM00421	B02	$1.63^{+0.25}_{-0.61}$	$2.03^{+0.51}_{-0.09}$	$0.43^{+0.19}_{-0.01}$				291.7 (311)	0.0
XMM00497	B02+L	$12.78^{+3.11}_{-0.87}$	2.0^f	$6.12^{+1.32}_{-0.44}$		$3.19^{+0.04}_{-0.05}$	$0.17^{+0.10}_{-0.10}$	638.0 (656)	0.0
XMM00860	B02	$3.37^{+2.39}_{-1.70}$	$2.02^{+0.51}_{-0.48}$	$0.37^{+0.25}_{-0.14}$				226.8 (233)	0.0
XMM01034	B02	$1.44^{+1.25}_{-0.38}$	2.0^f	$0.26^{+0.07}_{-0.04}$				225.2 (232)	0.0
XMM01279	B02	$1.63^{+0.09}_{-0.60}$	2.0^f	$1.51^{+0.02}_{-0.31}$				506.4 (616)	0.0
XMM01464	B02	$1.02^{+0.78}_{-0.02}$	$1.93^{+0.28}_{-0.09}$	$0.47^{+0.12}_{-0.02}$				412.3 (479)	0.0
XMM01723	B02+cpl+L	$17.91^{+39.73}_{-9.71}$	2.0^f	$0.95^{+1.64}_{-0.46}$	$0.06^{+0.08}_{-0.04}$	$3.08^{+0.01}_{-0.07}$	$0.13^{+0.45}_{-0.11}$	200.6 (171)	0.0
XMM01731	B02	$7.02^{+2.48}_{-4.25}$	$2.40^{+0.16}_{-0.83}$	$0.80^{+0.25}_{-0.42}$				239.3 (238)	0.0
XMM01740	B02	$6.23^{+12.03}_{-4.60}$	2.0^f	$0.20^{+0.17}_{-0.08}$				110.0 (127)	0.0
XMM02186	B02	$1.63^{+0.46}_{-0.60}$	$2.06^{+0.43}_{-0.37}$	$0.66^{+0.25}_{-0.17}$				118.0 (154)	0.0
XMM02347	B02	$4.07^{+2.12}_{-1.61}$	2.0^f	$0.39^{+0.10}_{-0.09}$				265.6 (264)	0.0
XMM02660	B02	$5.64^{+3.51}_{-2.09}$	$1.87^{+0.55}_{-0.33}$	$0.83^{+0.62}_{-0.26}$				245.4 (287)	0.0
XMM03098	B02	$1.63^{+1.20}_{-0.59}$	2.0^f	$0.29^{+0.08}_{-0.04}$				211.1 (238)	0.0
XMM03153	B02	$2.23^{+2.90}_{-1.12}$	$1.73^{+0.31}_{-0.18}$	$0.37^{+0.12}_{-0.05}$				356.8 (376)	0.0
XMM03342	B02	$1.63^{+2.28}_{-0.57}$	$2.27^{+0.30}_{-0.50}$	$0.23^{+0.16}_{-0.06}$				141.3 (130)	0.0
XMM03798	B02	$4.83^{+2.05}_{-2.28}$	$2.29^{+0.27}_{-0.50}$	$0.69^{+0.25}_{-0.26}$				221.7 (248)	0.0
XMM03900	B02	$5.45^{+1.53}_{-1.11}$	2.0^f	$1.73^{+0.28}_{-0.21}$				573.3 (637)	0.0
XMM03916	B02+L	$120.86^{+110.09}_{-30.26}$	2.0^f	$2.56^{+5.29}_{-1.00}$		$1.49^{+0.20}_{-0.13}$	$0.26^{+0.76}_{-0.22}$	171.5 (165)	0.30
XMM04259	B02	$13.56^{+16.78}_{-4.24}$	$1.76^{+0.78}_{-0.25}$	$0.54^{+1.36}_{-0.17}$				192.0 (212)	0.0
XMM04404	B02	$1.03^{+0.03}_{-0.03}$	$1.89^{+0.05}_{-0.01}$	$0.55^{+0.01}_{-0.01}$				327.7 (386)	0.0
XMM04475	B02	$1.63^{+5.84}_{-0.54}$	2.0^f	$0.13^{+0.09}_{-0.02}$				308.4 (305)	0.0
XMM04583	B02	$3.55^{+1.14}_{-0.93}$	2.0^f	$1.14^{+0.26}_{-0.22}$				412.6 (462)	0.0
XMM04804	B02	$3.73^{+2.67}_{-2.00}$	$2.02^{+0.50}_{-0.44}$	$0.50^{+0.31}_{-0.18}$				224.9 (234)	0.0
XMM04899	B02	$8.81^{+3.83}_{-2.15}$	2.0^f	$0.81^{+0.23}_{-0.14}$				295.4 (328)	0.0

Notes - Column (1): Source XIDs, Column (2): the best-fit model where B02 represents TBABS×(BORUS02 + ZTBABS×CABS×CUTOFFPL), and cpl represents an additional CUTOFFPL accounting for the scattered X-ray emission, Column (3): line-of-sight column density, Column (4): photon index, Column(5): normalisation of the transmitted cutoff power law component, Column(6): normalisation of the scattered cutoff power law component, Column (7) Fe Kα line energy at the observed−frame, Column (8): equivalent width of Fe Kα line, Column (9): the best-fit Cash statistics and degrees of freedom, Column (10): MCMC-based probability of source being a CT-AGN.

Table 4. Comparison of various parameters

Reference	No. of DOGs	Redshift (z)	$S_{24\,\mu m}$ (mJy)	$m_{\rm r}$ (mag)	$N_{\rm H}$ $(10^{22}\,{\rm cm}^{-2})$	$\log L_{2-10\,{\rm keV}}^{\rm int}$ (erg s^{-1})
(1)	(2)	(3)	(4)	(5)	(6)	(7)
1	34	$0.586-4.65\ (1.75)$	$0.39-8.11\ (0.81)$	$22.64-25.94\ (24.68)$	$1.02-120.86\ (3.29)$	$43.30-45.79(44.45)$
2	14	$1.22-5.22\ (2.29)$	$0.08-1.08\ (0.24)$	$24.51-27.01\ (26.34)$	$0.80-900.0\ (17.0)$	$41.50-44.82\ (43.57)$
3	10	$2.085-2.658\ (2.503)$	$1.92-19.16\ (7.50)$	$20.76-22.37\ (22.07)$	$1.00-8.0\ (1.95)$	$44.10-45.60\ (45.10)$
4	6	$0.282-1.023\ (0.775)$	$9.02-16.19\ (16.07)$	$18.22-21.56\ (21.29)$	$4.10-67.20\ (18.10)$	$43.30-45.30\ (44.20)$

Note: Reference - 1 - This work; 2 - Corral et al. (2016); 3 - Lansbury et al. (2020); 4 - Zou et al. (2020). The IR fluxes given in column (4) for references 3 and 4 are from WISE 22 μm band.

5 RESULTS AND DISCUSSION

5.1 Absorbing column densities

One of the main objectives of our study is to constrain the line-of-sight absorbing column densities ($N_{\rm H}$) in DOGs and estimate the fraction of CT-AGN in them. For our DOGs, we obtained $N_{\rm H}$ by modelling their $0.5−10$ keV X-ray spectra using two different models, *i.e.,* absorbed power law and BORUS02. We find that both models provide nearly similar $N_{\rm H}$ estimates (see Figure 1). We prefer to use $N_{\rm H}$ estimates derived from the BORUS02 model, considering the fact that it accounts for Compton scattering, as well as reprocessing of X-ray emission. We find that our sample DOGs have $N_{\rm H}$ in the range of 1.02×10^{22} cm^{-2} to 1.21×10^{24} cm^{-2} with a median value of 3.29×10^{22} cm^{-2} (see Table 4). There are only 06/34 (17.6 per cent) sources which can be classified as heavily obscured AGN with $N_{\rm H} > 10^{23}$ cm^{-2}, and the remaining DOGs show only moderate level obscuration (10^{22} cm$^{-2} \leq N_{\rm H} \leq 10^{23}$ cm^{-2}). We note that the $N_{\rm H}$ estimates in our sample DOGs are broadly consistent with other samples of DOGs reported in the literature (e.g., Corral et al. 2016; Lansbury et al. 2020; Zou et al. 2020).

In Table 4, we present a comparison of $N_{\rm H}$ and other parameters, *i.e.,* redshift, 24 μm flux, optical $r−$band magnitude, and absorption corrected $2.0−10$ keV X-ray luminosity of our DOGs with those reported in the literature. We caution that despite apparently similar $N_{\rm H}$ estimates found in different samples of DOGs, we need to account for the inherent biases in the samples and differences in the spectral quality. For instance, Corral et al. (2016) derived $N_{\rm H}$ for a sample of 14 DOGs in the CDFS using 6 Ms deep *Chandra* observations and an additional 3 Ms *XMM-Newton* data for 07/14 sources. They demonstrated that, for the same set of sources, better quality spectra often render significantly higher $N_{\rm H}$ than that derived from their low counts spectra presented in Georgantopoulos et al. (2011). We find that $N_{\rm H}$ estimates for relatively bright DOGs reported in Zou et al. (2020) and Lansbury et al. (2020) are somewhat lower than that found in our sample. We point out that Zou et al. (2020) performed X-ray spectral study of six relatively bright nearby ($0.3 < z < 1.0$) DOGs using *Chandra* snapshot observations with only 3 ks exposure time for each source, and they found only moderately obscured AGN (4.1×10^{22} cm$^{-2} \leq N_{\rm H} \leq 6.7 \times 10^{23}$ cm^{-2}; see Table 4). Lansbury et al. (2020) also used relatively low exposure (nearly $10−30$ ks exposure time) *XMM-Newton* observations for a sample of ten heavily dust-reddened quasars and found $N_{\rm H}$ in the range of 1×10^{22} cm$^{-2} − 8 \times 10^{22}$ cm^{-2}. We caution that a robust comparison of $N_{\rm H}$ across different samples of DOGs warrants sufficiently good-quality spectra. Although, lower obscuration can also be attributed to sample biases such as sources belonging to late evolutionary stages (see Section 5.4).

5.2 Compton-thick AGN in DOGs

In our sample, we found only one source (XMM03916) with $N_{\rm H} = 1.21 \times 10^{24}$ cm^{-2}, which can be classified as CT-AGN candidate. To confirm the CT nature, we applied the Markov Chain Monte Carlo (MCMC) parameter estimation techniques on the best fits of all our sample sources and obtained the probability distribution function (PDF) of $N_{\rm H}$. To
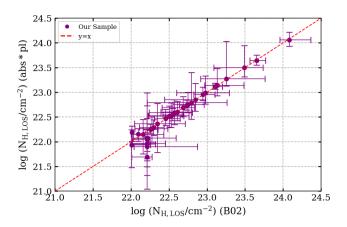

Figure 1. The comparison of $N_{\rm H}$ obtained from two different models, *i.e.,* absorbed power law and BORUS02 models.

perform the MCMC, we used the Goodman–Weare algorithm (Goodman & Weare 2010) within the XSPEC. For robust estimation of the parameter space, we used 20 walkers and 10^4 steps in the MCMC and derived $N_{\rm H}$ PDFs for each sample source. Using the MCMC on both the absorbed power law and the BORUS02 model best fits, we derived the probability of being CT-AGN ($P_{\rm CT}$) for each source (see Table 2 and Table 3). We find that, as expected, only XMM03916 shows non-zero probability of being CT-AGN with $P_{\rm CT}$ values of 0.12 and 0.30 obtained from the power law and BORUS02 best fits, respectively. The $N_{\rm H}$ PDF of XMM03916, a CT-AGN candidate, is shown in Figure A5. The fraction of CT-AGN candidates in our sample is only (01/34) 3.0 per cent. We note that the comparison of CT-AGN fraction among the different samples of DOGs may not be straightforward due to the small number statistics and inherent sample biases. We point out that using low-count X-ray spectra Zou et al. (2020) and Lansbury et al. (2020) found no CT-AGN in their small samples of relatively bright DOGs. However, using deep *Chandra* and *XMM-Newton* observations, Corral et al. (2016) found (3/14) 21 per cent of their sample sources as CT-AGN. The fraction of CT-AGN in deep X-ray surveys has been limited to nearly 10 per cent (see Lanzuisi et al. 2015, 2018; Marchesi et al. 2016; Masini et al. 2018; Li et al. 2019), which is also higher than that found in our study.

Further, we compare our heavily obscured sources with those reported by Yan et al. (2023) who used Bayesian spectral analysis and identified 12 CT-AGN and 58 heavily obscured AGN ($23.70 \leq \log N_{\rm H} < 24.17$) among all the X-ray detected sources in the XMM-SERVS coverage of the XMM-LSS. Since our DOGs are gleaned from the X-ray detected sources in the same field, one can expect a significant overlap between the two samples. Surprisingly, none except one (XMM00497) of our sample sources is found among the CT-AGN and heavily obscured AGN reported in Yan et al. (2023). Our CT-AGN candidate XMM03916 is not identified as either CT-AGN or heavily obscured AGN in their study. This discrepancy can be attributed to several factors that include differences in spectral model, redshift, spectral quality and posterior $N_{\rm H}$ probability cutoff limit. We point out that, to all their sample sources, Yan et al. (2023) uniformly used a model which can be expressed as A⋆PHABS⋆(BORUS02 + ZPHABS⋆CABS⋆CUTOFFPL + B⋆CUTOFFPL) in the XSPEC.

This model is fairly similar to our borus02 model except for the additional scattered component modelled with cut-off power law considered for all the sources. In our study, we find that the addition of the scattered power law component provides marginal improvement in the fit statistics of only one of our sample sources (see Table 3). Further, unlike Yan et al. (2023), who used photo−z based on the forced photometry (Zou et al. 2022), we used photo−z derived from the Tractor image-modelling software-based de-blended multi-band forced photometry across 13 optical to near-IR bands (Nyland et al. 2023), which are considered to be more accurate than previous estimates (e.g., Ni et al. 2021; Zou et al. 2022). For some of our sources, photo−z estimates from Nyland et al. (2023) and Zou et al. (2022) are substantially different. Also, to get the better spectral quality, we have added *Chandra* data, whenever available. It is worth pointing out that Yan et al. (2023) identified a source as CT-AGN or heavily obscured AGN only if its posterior $N_{\rm H}$ probability is > 50 per cent for the threshold $N_{\rm H}$ values set to 1.5×10^{24} cm^{-2} and 5×10^{23} cm^{-2} for CT-AGN and heavily obscured AGN, respectively. We note that the cutoff limit placed on the posterior $N_{\rm H}$ probability in Yan et al. (2023) is somewhat arbitrary and strict. Sources with posterior $N_{\rm H}$ probability < 50 per cent have only lesser chances of being CT-AGN/ heavily obscured AGN but cannot be completely ruled out. Lanzuisi et al. (2018) demonstrated the existence of a large number of CT-AGN with only 5 per cent of their posterior $N_{\rm H}$ probability above 10^{24} cm^{-2}. Akylas et al. (2016) identified 53/604 CT-AGN considering posterior $N_{\rm H}$ probability only ≥ 3.0 per cent. Therefore, it is fairly possible that our CT-AGN candidate and heavily obscured AGN are missed by Yan et al. (2023) due to a much higher cutoff limit (50 per cent) placed on the posterior $N_{\rm H}$ probability.

5.3 The 2.0−10 X-ray luminosity versus 6 μm MIR luminosity diagnostic plot

To further investigate the nature of the obscured AGN hosted in our DOGs, we exploit the correlation between 2.0−10 keV X-ray luminosity ($L_{2.0-10 \rm\ keV}$) and 6.0 μm mid-IR luminosity ($L_{6\ \mu m}$). Due to the heavy absorption, the observed X-ray luminosities of CT-AGN and obscured AGN are expected to get suppressed while their mid-IR luminosities remain nearly unaffected by the obscuring medium. Thus, $L_{2.0-10 \rm\ keV}$ − $L_{6\ \mu m}$ correlation is commonly used as a diagnostic to identify CT-AGN, which shows a large deviation with respect to the unobscured or less obscured AGN (Lanzuisi et al. 2018; Guo et al. 2021). In Figure 2 (*left panel*), we plot observed $L_{2.0-10 \rm\ keV}$ versus $L_{6\ \mu m}$ for our sample sources, as well as other different kinds of X-ray sources, *e.g.,* X-ray faint DOGs with no X-ray spectral analysis, CT-AGN from Yan et al. (2023), and X-ray detected sources from Chen et al. (2018) in the XMM-LSS field. To maintain uniformity with other X-ray sources, we obtained 2.0−10 keV luminosities from the absorbed power law model for our sample sources. For X-ray faint DOGs and X-ray sources, we obtained 2.0−10 keV flux from the XMM-SERVS catalogue (Chen et al. 2018). The 6.0 μm luminosities are taken from Zou et al. (2022) and these are available only for 30/34 of our sample DOGs, 42/55 X-ray faint DOGs, 1401 X-ray sources with spec−z, and 10 CT-AGN from Yan et al. (2023).

We compared our sources with the $L_{2.0-10 \rm\ keV}$ − $L_{6\ \mu m}$

correlation reported by Stern (2015), who probed it for a sample of radio-quiet AGN distributed across a wide range of X-ray luminosities (10^{42} erg s^{-1} − 10^{46} erg s^{-1}). The correlation can be expressed as $L_{2.0-10 \rm\ keV} = 40.981 + 1.024x - 0.047x^2$, where $x = \log(\nu L_\nu (6\ \mu m)/10^{41}$ erg s^{-1}), and $L_{2.0-10 \rm\ keV}$ is in the units of erg s^{-1}. We find that our CT-AGN candidate XMM03916 as well as CT-AGN reported in Yan et al. (2023) show 3σ or larger deviation from the $L_{2.0-10 \rm\ keV}$ − $L_{6\ \mu m}$ correlation curve. Our DOGs with moderate absorption seem to be consistent with the $L_{2.0-10 \rm\ keV}$ − $L_{6\ \mu m}$ correlation within 1σ deviation. Thus, the CT-AGN candidate identified in our sample is consistent with the $L_{2.0-10 \rm\ keV}$ − $L_{6\ \mu m}$ correlation diagnostic. We note that, in comparison to the CT-AGN reported in Yan et al. (2023), our DOGs are systematically more luminous both in X-ray as well as at 6.0 μm (see Figure 2). The systematically high luminosities of our sample DOGs can be attributed to their much higher redshifts ($0.586 \le z \le 4.65$ with a median value of 1.75) than that for CT-AGN ($0.058 \le z \le 1.98$ with a median value of 1.03).

We also overplotted the absorption-corrected X-ray luminosities of our sample sources and CT-AGN on the $L_{2.0-10 \rm\ keV}$ − $L_{6\ \mu m}$ correlation (see Figure 2, right panel). As expected, all of our sample DOGs, as well as CT-AGN lie on the $L_{2.0-10 \rm\ keV}$ − $L_{6\ \mu m}$ correlation curve mostly within 1σ deviation once their X-ray luminosities are corrected for absorption. This further confirms the veracity of $N_{\rm H}$ estimates in our sample sources. Based on the absorption-corrected X-ray luminosities, which span across 2.00×10^{43} erg s$^{-1} \le L_{2.0-10 \rm\ keV} \le 6.17 \times 10^{45}$ erg s^{-1}, our sample DOGs can be classified as highly luminous quasars with varying levels of obscuration around them.

5.4 $N_{\rm H}$ versus Eddington ratios: Evolutionary scenario of AGN in DOGs

Since our DOGs host highly luminous AGN, the surrounding obscuring material is likely to be affected by the radiative feedback. To gain insights into the evolutionary stage of AGN hosted in our DOGs, we exploited the $N_{\rm H}$ versus Eddington ratio ($\lambda_{\rm Edd}$) diagnostic plot. In Figure 3, we plot the $N_{\rm H}$ versus $\lambda_{\rm Edd}$ for our sample DOGs, as well as DOGs reported in the literature (Corral et al. 2016; Ricci et al. 2017; Zou et al. 2020; Lansbury et al. 2020). For our sample sources, we estimated $\lambda_{\rm Edd} = \frac{L_{\rm bol}}{1.26 \times 10^{38}\ M_{\rm BH}}$; where bolometric luminosity ($L_{\rm bol}$) is measured in the units of erg s^{-1} and black hole mass ($M_{\rm BH}$) in the units of $M_\odot$. We obtained $L_{\rm bol}$ estimates from $L_{2-10 \rm\ keV}$ using $L_{\rm bol} = K_x L_{2-10 \rm\ keV}$ correlation (Duras et al. 2020), where the bolometric correction factor K_x is given by

$$K_x = a \left[1 + \left(\frac{\log(L_{2-10 \rm\ keV}/L_\odot)}{b} \right)^c \right]$$

where, $a = 15.33$, $b = 11.48$ and $c = 16.20$. Since black hole masses of our DOGs are not available, we assume $M_{\rm BH} = 10^{8.5}\ M_\odot$, which is an average value for DOGs reported by Zou et al. (2020). To account for the deviation of the actual value of $M_{\rm BH}$ from the average value, we consider $10^8\ M_\odot$ − $10^9\ M_\odot$ range for $M_{\rm BH}$. The large error bars introduced in $\lambda_{\rm Edd}$ correspond to the range of $M_{\rm BH}$, and these are much larger than that contributed by the errors in X-ray luminosities.

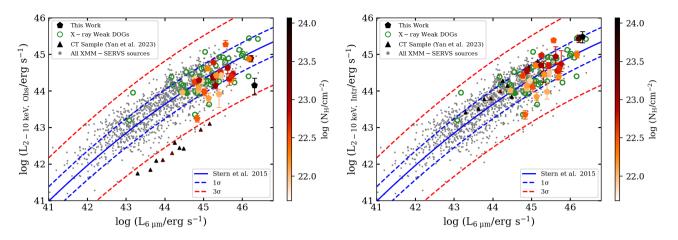In the $N_{\rm H}$ versus $\lambda_{\rm Edd}$ plot, we show different regions, *i.e.,*

Figure 2. *Left panel*: The plot of observed 2.0−10 keV X-ray luminosity ($L_{2.0−10\ \mathrm{keV}}$) versus mid-IR 6 μm luminosity ($L_{6.0\ \mu m}$) for various types of X-ray detected AGN. *Right panel*: Same as the left panel plot except for absorption-corrected 2.0−10 keV X-ray luminosities ($L_{2.0−10\ \mathrm{keV}}$) are plotted for our sample sources and CT-AGN from Yan et al. (2023). Our sample DOGs are shown with filled pentagon symbols. The X-ray faint DOGs with no X-ray spectral analysis are shown with green open circles. The X-ray sources from Chen et al. (2018) are shown with grey dots. The CT-AGN reported in Yan et al. (2023) are shown with triangles. The line-of-sight column densities, whenever available, are indicated with a colour bar. The blue solid curve represents the $L_{2.0−10\ \mathrm{keV}} − L_{6.0\ \mu m}$ correlation reported by Stern et al. 2015. The blue dashed and red dashed curves on either side represent 1σ and 3σ dispersion, respectively, for the X-ray source population reported by Chen et al. (2018).

blowout region having short-lived obscuration region, long-lived obscuration region, and host-galaxy dust lanes caused obscuration region. The tracks segregating short-lived and long-lived obscuring regions represent the effective column density (N_{H}) around AGN characterised with λ_{Edd}. The solid and dotted tracks are obtained by assuming single scattering (Fabian et al. 2009) and radiation trapping (Ishibashi et al. 2018) of photons emitted from the AGN, respectively. The circumnuclear material is expected to undergo a fast blowout phase if column densities are lower, and hence resulting in AGN to lie in the blowout region. The obscuration is likely to sustain against outflows, which in turn results in long-lived obscuration around AGN, if column densities are much higher.

From Figure 3, it is evident that the most of our DOGs, irrespective of their obscuration level, lie in the blowout region. Thus, obscuration in our DOGs is short-lived and they are likely to evolve into unobscured AGN. The 04/34 ($\sim$ 11.7 per cent) of our DOGs showing super Eddington accretion rates and high obscuration ($N_{\mathrm{H}} > 10^{23}$ cm^{-2}) can be Hot DOGs, which are known to exhibit higher obscuration than reddened quasars (Vito et al. 2018). Hot DOGs supposedly belong to an early phase of evolution during which accretion peaks, but the feedback is yet to blow out the surrounding reservoir of gas and dust. In contrast, reddened quasars belong to a later phase during which feedback is dominantly ongoing. Further, reddened quasars can show different levels of X-ray obscuration depending upon their evolutionary stages (Goulding et al. 2018). In other words, reddened quasars can represent a heterogeneous population belonging to an early evolutionary phase just after the Hot DOGs, as well as a late phase during which radiative feedback has swept away surrounding material. From the N_{H} versus λ_{Edd} plot, we conclude that all but four of our DOGs belong to the intermediate to late evolutionary phase, during which dominant AGN feedback has blown away most of the surrounding obscuring material.
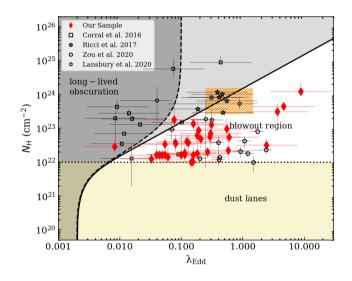

Figure 3. The N_{H} versus Eddington ratio plot for our sample DOGs. The DOGs and reddened quasars reported in the literature (Corral et al. 2016; Ricci et al. 2017; Zou et al. 2020; Lansbury et al. 2020) are also plotted. The grey-shaded region represents region for long-lived obscuration. The solid curve and dashed curve segregating long-lived obscuration and short-lived obscuration are based on single-scattering limit and radiation-trapping limit, respectively (Ishibashi et al. 2018). The yellow-shaded region with low absorption represents obscuration caused by host galaxy dust lanes. The orange-shaded region belongs to Hot DOGs reported in Vito et al. (2018); Wu et al. (2018).

6 CONCLUSIONS

In this work, we present the X-ray spectral properties of 34 DOGs using deep *XMM-Newton* observations in the XMM-SERVS coverage of the XMM-LSS field. To achieve better-quality spectra, we combined all the archival *XMM-Newton* pn and MOS observations, and utilised *Chandra*/ACIS ob-

servations, whenever available. Our conclusions are outlined as below.

• We find that the $0.5-10$ keV X-ray spectra of our DOGs can be fitted with a simple absorbed power law as well as with BORUS02, a physical model assuming toroidal geometry of the obscuring material around AGN. Both the models give similar absorbing column densities and photon indices. In one of our sample sources, an additional scattered component is also required to obtain the best fit.

• The line-of-sight absorbing column densities in our DOGs span across a wide range from 1.02×10^{22} cm^{-2} to 1.21×10^{24} cm^{-2} with a median value of 3.29×10^{22} cm^{-2}. Nearly $06/34$ (17.6 per cent) of our sample sources can be classified as heavily obscured AGN with $N_{\rm H} > 1.0 \times 10^{23}$ cm^{-2}. Thus, AGN hosted in DOGs show varying levels of obscuration ranging from moderately obscured AGN to CT-AGN.

• In our work, we identified one new CT-AGN candidate XMM03916 which have $N_{\rm H} > 1.1 \times 10^{24}$ cm^{-2} and posterior probability of being CT-AGN ($P_{\rm CT}$) 0.30. As expected, our CT-AGN candidate follows $L_{2.0-10 \rm\ keV} - L_{6\ \mu m}$ correlation once the X-ray luminosity is corrected for absorption. The consistency between our CT-AGN candidate and previously identified CT-AGN provides further confirmation of its CT nature.

• The fraction of CT-AGN candidates in our sample is merely $01/34 = 3.0$ per cent, which is lower than that (nearly 10 per cent) found in the deep X-ray surveys (Marchesi et al. 2016; Lanzuisi et al. 2018; Li et al. 2019). We caution that the moderate to poor spectral quality and inherent sample biases may affect the fraction of CT-AGN.

• The AGN hosted in our DOGs are found to be highly luminous with their absorption-corrected X-ray luminosities spanning across 2.00×10^{43} erg s^{-1} to 6.17×10^{45} erg s^{-1} with a median value of 2.82×10^{44} erg s^{-1}, which suggest them to be luminous quasars.

• In the $N_{\rm H}$ versus $\lambda_{\rm Edd}$ diagnostic plot, most of our DOGs belong to the blowout region, suggesting a short-lived obscuration. We find that all but four of our DOGs show similarity with reddened quasars. The four DOGs with super Eddington accretion and high obscuration, are likely to be Hot DOGs, which belong to an early evolutionary phase during which accretion as well as obscuration peaks. Thus, on the basis of $N_{\rm H}$ versus $\lambda_{\rm Edd}$ diagnostic plot, we conclude that our DOGs are likely to represent a heterogeneous population belonging to the early to late evolutionary phases.

FACILITIES

XMM-Newton, *Chandra*, *Subaru* and *Spitzer*

DATA AVAILABILITY

The *XMM-Newton* and *Chandra* data are publicly available from the archives of HEASARC maintained by NASA.

REFERENCES

Aihara H., et al., 2018, PASJ, 70, S4
Akylas A., Georgakakis A., Georgantopoulos I., Brightman M., Nandra K., 2012, A&A, 546, A98
Akylas A., Georgantopoulos I., Ranalli P., Gkiokas E., Corral A., Lanzuisi G., 2016, A&A, 594, A73
Alexander D. M., Hickox R. C., 2012, New Astron. Rev., 56, 93
Ananna T. T., et al., 2019, ApJ, 871, 240
Antonucci R. R. J., Miller J. S., 1985, ApJ, 297, 621
Arnaud K. A., 1996, in Jacoby G. H., Barnes J., eds, Astronomical Society of the Pacific Conference Series Vol. 101, Astronomical Data Analysis Software and Systems V. p. 17
Arnouts S., Cristiani S., Moscardini L., Matarrese S., Lucchin F., Fontana A., Giallongo E., 1999, MNRAS, 310, 540
Assef R. J., et al., 2020, ApJ, 897, 112
Baldwin J. A., 1977, ApJ, 214, 679
Baloković M., et al., 2018, ApJ, 854, 42
Bianchi S., Maiolino R., Risaliti G., 2012, Advances in Astronomy, 2012, 782030
Boorman P. G., Gandhi P., Baloković M., Brightman M., Harrison F., Ricci C., Stern D., 2018, MNRAS, 477, 3775
Bradshaw E. J., et al., 2013, MNRAS, 433, 194
Burlon D., Ajello M., Greiner J., Comastri A., Merloni A., Gehrels N., 2011, ApJ, 728, 58
Bussmann R. S., et al., 2009, ApJ, 705, 184
Cappelluti N., et al., 2009, A&A, 497, 635
Cash W., 1979, ApJ, 228, 939
Chen C. T. J., et al., 2018, MNRAS, 478, 2132
Chiappetti L., et al., 2005, A&A, 439, 413
Coil A. L., et al., 2011, ApJ, 741, 8
Comastri A., 2004, in Barger A. J., ed., Astrophysics and Space Science Library Vol. 308, Supermassive Black Holes in the Distant Universe. p. 245 (arXiv:astro-ph/0403693), doi:10.1007/978-1-4020-2471-9_8
Corral A., et al., 2016, A&A, 592, A109
Coupon J., et al., 2009, A&A, 500, 981
Dawson K. S., et al., 2013, AJ, 145, 10
Desprez G., et al., 2023, A&A, 670, A82
Dey A., et al., 2008, ApJ, 677, 943
Duras F., et al., 2020, A&A, 636, A73
Elitzur M., 2006, New Astron. Rev., 50, 728
Fabian A. C., Vasudevan R. V., Mushotzky R. F., Winter L. M., Reynolds C. S., 2009, MNRAS, 394, L89
Farrah D., et al., 2017, ApJ, 844, 106
Fiore F., et al., 2008, ApJ, 672, 94
Fiore F., et al., 2009, ApJ, 693, 447
Fukazawa Y., et al., 2011, ApJ, 727, 19
Garilli B., et al., 2014, A&A, 562, A23
Georgantopoulos I., Georgakakis A., Rowan-Robinson M., Rovilos E., 2008, A&A, 484, 671

Georgantopoulos I., Rovilos E., Xilouris E. M., Comastri A., Akylas A., 2011, A&A, 526, A86

George I. M., Fabian A. C., 1991, MNRAS, 249, 352

Gilli R., Comastri A., Hasinger G., 2007, A&A, 463, 79

Glikman E., LaMassa S., Piconcelli E., Urry M., Lacy M., 2017, ApJ, 847, 116

Glikman E., LaMassa S., Piconcelli E., Zappacosta L., Lacy M., 2024, MNRAS,

Goodman J., Weare J., 2010, Communications in Applied Mathematics and Computational Science, 5, 65

Goulding A. D., et al., 2018, ApJ, 856, 4

Granato G. L., De Zotti G., Silva L., Bressan A., Danese L., 2004, ApJ, 600, 580

Guo X., Gu Q., Ding N., Yu X., Chen Y., 2021, ApJ, 908, 169

Heywood I., Hale C. L., Jarvis M. J., Makhathini S., Peters J. A., Sebokolodi M. L. L., Smirnov O. M., 2020, MNRAS, 496, 3469

Hopkins P. F., Hernquist L., Cox T. J., Di Matteo T., Robertson B., Springel V., 2006, ApJS, 163, 1

Hopkins P. F., Hernquist L., Cox T. J., Kereš D., 2008, ApJS, 175, 356

Ilbert O., et al., 2006, A&A, 457, 841

Ishibashi W., Fabian A. C., Ricci C., Celotti A., 2018, MNRAS, 479, 3335

Iwasawa K., Taniguchi Y., 1993, ApJ, 413, L15

Iwasawa K., et al., 2012, A&A, 537, A86

Jarvis M. J., et al., 2013, MNRAS, 428, 1281

Kayal A., Singh V., Chandra C. H. I., Wadadekar Y., Dutta S., 2022, Journal of Astrophysics and Astronomy, 43, 84

Koss M. J., et al., 2016, ApJ, 825, 85

LaMassa S. M., et al., 2016, ApJ, 820, 70

Laloux B., et al., 2023, MNRAS, 518, 2546

Lansbury G. B., Banerji M., Fabian A. C., Temple M. J., 2020, MNRAS, 495, 2652

Lanzuisi G., Piconcelli E., Fiore F., Feruglio C., Vignali C., Salvato M., Gruppioni C., 2009, A&A, 498, 67

Lanzuisi G., et al., 2015, A&A, 573, A137

Lanzuisi G., et al., 2018, MNRAS, 480, 2578

Le Fèvre O., et al., 2013, A&A, 559, A14

Li J., et al., 2019, ApJ, 877, 5

Lonsdale C. J., et al., 2003, PASP, 115, 897

Magdziarz P., Zdziarski A. A., 1995, MNRAS, 273, 837

Maiolino R., Salvati M., Bassani L., Dadina M., della Ceca R., Matt G., Risaliti G., Zamorani G., 1998, A&A, 338, 781

Marchesi S., et al., 2016, ApJ, 830, 100

Marconi A., Risaliti G., Gilli R., Hunt L. K., Maiolino R., Salvati M., 2004, MNRAS, 351, 169

Martínez-Sansigre A., et al., 2007, MNRAS, 379, L6

Masini A., et al., 2018, ApJS, 235, 17

Matt G., Iwasawa K., 2019, MNRAS, 482, 151

Matt G., Fabian A. C., Guainazzi M., Iwasawa K., Bassani L., Malaguti G., 2000, MNRAS, 318, 173

Mauduit J. C., et al., 2012, PASP, 124, 714

McLure R. J., et al., 2013, MNRAS, 428, 1088

Melbourne J., et al., 2012, AJ, 143, 125

Menzel M. L., et al., 2016, MNRAS, 457, 110

Momcheva I. G., et al., 2016, ApJS, 225, 27

Narayanan D., et al., 2010, MNRAS, 407, 1701

Netzer H., 2015, ARA&A, 53, 365

Ni Q., et al., 2021, ApJS, 256, 21

Nyland K., et al., 2017, ApJS, 230, 9

Nyland K., Lacy M., Brandt W. N., Yang G., Ni Q., Sajina A., Zou F., Vaccari M., 2023, Research Notes of the American Astronomical Society, 7, 33

Oliver S. J., et al., 2012, MNRAS, 424, 1614

Pacaud F., et al., 2006, MNRAS, 372, 578

Pierre M., et al., 2016, A&A, 592, A1

Pope A., et al., 2008, ApJ, 689, 127

Ricci C., Ueda Y., Koss M. J., Trakhtenbrot B., Bauer F. E., Gandhi P., 2015, ApJ, 815, L13

Ricci C., et al., 2017, MNRAS, 468, 1273

Sanders D. B., Mirabel I. F., 1996, ARA&A, 34, 749

Schuldt S., Suyu S. H., Cañameras R., Taubenberger S., Meinhardt T., Leal-Taixé L., Hsieh B. C., 2021, A&A, 651, A55

Singh V., Shastri P., Risaliti G., 2011, A&A, 532, A84

Singh V., et al., 2014, A&A, 569, A52

Skelton R. E., et al., 2014, ApJS, 214, 24

Stern D., 2015, ApJ, 807, 129

Stern D., et al., 2014, ApJ, 794, 102

Suleiman N., et al., 2022, PASJ, 74, 1157

Tanaka M., et al., 2018, PASJ, 70, S9

Teng S. H., Veilleux S., 2010, ApJ, 725, 1848

Toba Y., et al., 2015, PASJ, 67, 86

Toba Y., et al., 2020, ApJ, 888, 8

Torres-Albà N., et al., 2021, ApJ, 922, 252

Tozzi P., et al., 2006, A&A, 451, 457

Treister E., Urry C. M., Virani S., 2009a, ApJ, 696, 110

Treister E., et al., 2009b, ApJ, 706, 535

Tsai C.-W., et al., 2015, ApJ, 805, 90

Ueda Y., et al., 2008, ApJS, 179, 124

Urry C. M., Padovani P., 1995, PASP, 107, 803

Vito F., et al., 2018, MNRAS, 474, 4528

Wu J., et al., 2018, ApJ, 852, 96

Yan W., et al., 2023, ApJ, 951, 27

Yutani N., Toba Y., Baba S., Wada K., 2022, arXiv e-prints, p. arXiv:2205.00567

Zappacosta L., et al., 2018, A&A, 618, A28

Zhao X., Marchesi S., Ajello M., Cole D., Hu Z., Silver R., Torres-Albà N., 2021, A&A, 650, A57

Zou F., Brandt W. N., Vito F., Chen C.-T., Garmire G. P., Stern D., Ayubinia A., 2020, MNRAS, 499, 1823

Zou F., et al., 2021, Research Notes of the American Astronomical Society, 5, 31

Zou F., et al., 2022, ApJS, 262, 15

APPENDIX A: THE X-RAY OBSERVATION DETAILS OF OUR DOGS

Table A1. The X-ray observations log of our DOGs.

XID	Obs ID	Obs Date	$T_{\rm obs}$	Total $T_{\rm exp}^{\rm eff}$	Total Counts$_{(0.5-10\ {\rm keV})}$
		(YYYY-MM-DD:Thh:mm:ss)	(ks)	(ks)	(cts)
(1)	(2)	(3)	(4)	(5)	(6)
XMM00059	0404967501	2007-01-09T18:45:25.0	18.9	70.8	695
	0404967901	2007-01-10T14:40:38.0	14.9		
	0553911601	2008-07-03T19:15:54.0	13.5		
	0742430301	2015-02-06T19:24:58.0	100.0		
XMM00131	0112370101	2000-07-31T21:49:26.0	61.4	86.5	535
	0112371001	2000-08-02T20:24:27.0	66.0		
	0112370601	2002-08-12T05:43:17.0	47.9		
XMM00136	0112370701	2002-08-08T15:05:39.0	49.6	46.5	176
	0404966501	2006-08-09T07:21:12.0	11.9		
XMM00191	0404967401	2007-01-08T14:06:49.0	15.0	70.8	385
	0404967501	2007-01-09T18:45:25.0	18.9		
	0404967901	2007-01-10T14:40:38.0	14.9		
	0553911601	2008-07-03T19:15:54.0	13.5		
	0742430301	2015-02-06T19:24:58.0	100.0		
XMM00205	0112371701	2000-08-08T04:37:14.0	39.6	58.2	125
	0112372001	2003-01-07T04:18:37.0	28.0		
	0404967001	2007-01-08T00:52:16.0	14.9		
XMM00250	0112371701	2000-08-08T04:37:14.0	39.6	53.8	173
	0112372001	2003-01-07T04:18:37.0	28.0		
	0404967001	2007-01-08T00:52:16.0	14.9		
XMM00267	0404967001	2007-01-08T00:52:16.0	14.9	79.7	1037
	0404967401	2007-01-08T14:06:49.0	15.0		
	0404967501	2007-01-09T18:45:25.0	18.9		
	0553911601	2008-07-03T19:15:54.0	13.5		
	0742430301	2015-02-06T19:24:58.0	100.0		
	0785100101	2016-07-01T15:53:31.0	22.5		
XMM00359	0404967401	2007-01-08T14:06:49.0	15.0	46.0	160
	0404967501	2007-01-09T18:45:25.0	18.9		
	0553911601	2008-07-03T19:15:54.0	13.5		
	0742430301	2015-02-06T19:24:58.0	100.0		
XMM00393	0112370101	2000-07-31T21:49:26.0	61.4	70.5	130
	0112371001	2000-08-02T20:24:27.0	66.0		
XMM00395	0112370101	2000-07-31T21:49:26.0	61.4	80.9	305
	0112371001	2000-08-02T20:24:27.0	66.0		
XMM00421	0112371701	2000-08-08T04:37:14.0	39.6	60.0	242
	0112372001	2003-01-07T04:18:37.0	28.0		
	0404967001	2007-01-08T00:52:16.0	14.9		
	0785100101	2016-07-01T15:53:31.0	22.5		
XMM00497	0112370701	2002-08-08T15:05:39.0	49.6	64.4	742
	0112370801	2002-08-09T05:29:19.0	50.8		
	0404966401	2006-07-31T02:38:25.0	11.9		
	0553911301	2008-08-10T10:08:41.0	13.7		
XMM00860	0112370401	2000-08-06T05:12:57.0	46.8	79.5	129
	0112371501	2000-08-06T20:08:34.0	11.8		
	0404966901	2007-01-07T18:38:27.0	19.9		
	0553911501	2009-01-01T17:29:55.0	15.0		
	0785100101	2016-07-01T15:53:31.0	22.5		
	0785100301	2016-07-02T20:09:16.0	26.1		
	0793580101	2017-01-02T14:22:49.0	28.0		
XMM01034	0112370401	2000-08-06T05:12:57.0	46.8	62.4	146
	0112371501	2000-08-06T20:08:34.0	11.8		
	0404966901	2007-01-07T18:38:27.0	19.9		
	0553911501	2009-01-01T17:29:55.0	15.0		
	0785100101	2016-07-01T15:53:31.0	22.5		
	0785100301	2016-07-02T20:09:16.0	26.1		
	0793580101	2017-01-02T14:22:49.0	28.0		

Notes - Column (1): X-ray source ID from the XMM-SERVS catalogue reported by Chen et al. (2018), Column (2): observation IDs of *XMM-Newton* and *Chandra* observations, '(Ch)' indicates *Chandra* observations, Column (3): Observation dates for the corresponding observation IDs, Column (4): Observation times in ks for each observation IDs; Column (5): The sum of effective exposure times from each observation IDs; Column (6): The total number of counts in 0.5−10 keV band.

Table A1. The X-ray observations log of our DOGs.

XID	Obs ID	Obs Date (YYYY-MM-DD:Thh:mm:ss)	$T_{\rm obs}$ (ks)	Total $T_{\rm exp}^{\rm eff}$ (ks)	Total Counts$_{(0.5-10\ \rm keV)}$ (cts)
(1)	(2)	(3)	(4)	(5)	(6)
XMM01279	0112370301	2000-08-04T20:16:28.0	66.0	76.1	565
	0112370401	2000-08-06T05:12:57.0	46.8		
	0112371501	2000-08-06T20:08:34.0	11.8		
	0785100801	2016-07-05T01:04:36.0	23.0		
	0793580301	2017-01-01T10:04:38.0	9.0		
	0793580101	2017-01-02T14:22:49.0	28.0		
	0780452301	2017-02-09T11:06:48.0	24.1		
XMM01464	0112370301	2000-08-04T20:16:28.0	66.0	85.9	531
	0404966601	2007-01-06T14:04:02.0	13.9		
	0785100801	2016-07-05T01:04:36.0	23.0		
	0780452401	2017-02-09T18:08:28.0	23.0		
	14348 (Ch)	2011-10-03T09:28:05	63.7		
	13374 (Ch)	2011-10-07T05:41:46	75.7		
XMM01723	0037982001	2002-08-14T13:52:03.0	17.8	52.7	101
	0785100501	2016-07-03T10:23:26.0	22.0		
	0785100801	2016-07-05T01:04:36.0	23.0		
	0785101201	2016-07-06T03:57:56.0	25.9		
	0793580301	2017-01-01T10:04:38.0	9.0		
	0793580801	2017-01-16T20:33:01.0	18.0		
XMM01731	0147111301	2003-07-24T09:02:34.0	12.9	51.9	137
	0404966601	2007-01-06T14:04:02.0	13.9		
	0785101101	2016-07-05T21:22:56.0	22.5		
	0793580701	2017-01-03T08:02:49.0	16.0		
	0780452401	2017-02-09T18:08:28.0	23.0		
	14348 (ch)	2011-10-03T09:28:05	63.7		
	13374 (ch)	2011-10-07T05:41:46	75.7		
XMM01740	0147111301	2003-07-24T09:02:34.0	12.9	60.8	47
	0404966601	2007-01-06T14:04:02.0	13.9		
	0785100801	2016-07-05T01:04:36.0	23.0		
	0785101101	2016-07-05T21:22:56.0	22.5		
	0793580701	2017-01-03T08:02:49.0	16.0		
	0793580801	2017-01-16T20:33:01.0	18.0		
	14348 (Ch)	2011-10-03T09:28:05	63.7		
	13374 (Ch)	2011-10-07T05:41:46	75.7		
XMM02186	0037982501	2003-01-25T01:19:09.0	14.1	33.7	109
	0037982401	2003-01-25T05:51:41.0	18.9		
	0037982201	2003-01-28T19:15:43.0	16.4		
	0404960601	2006-07-07T03:36:58.0	11.9		
	0785101501	2016-07-07T14:16:31.0	22.0		
	0793581001	2017-01-04T20:54:08.0	9.0		
XMM02347	0147111501	2003-07-24T17:12:34.0	11.0	65.9	163
	0404960401	2006-07-06T19:43:38.0	11.9		
	0785101001	2016-07-05T14:47:56.0	22.5		
	0785101101	2016-07-05T21:22:56.0	22.5		
	0785101601	2016-07-07T20:55:41.0	22.0		
	0793580701	2017-01-03T08:02:49.0	16.0		
	0793581101	2017-01-04T23:56:38.0	9.0		
XMM02660	0109520501	2001-07-03T22:44:36.0	24.8	65.6	226
	0112680801	2002-01-31T20:21:47.0	15.6		
	0785101701	2016-07-08T03:22:21.0	27.4		
	0785101801	2016-07-29T05:19:31.0	22.0		
	0780450201	2016-08-13T23:26:35.0	17.0		
	0793581201	2017-01-01T12:54:38.0	35.0		
XMM03098	0109520601	2002-01-31T13:04:39.0	23.6	66.0	166
	0112680501	2002-07-25T16:24:58.0	23.6		
	0780450301	2016-08-14T04:29:55.0	17.0		
	0780450601	2016-08-14T14:36:35.0	17.0		
	0780452201	2017-01-07T17:07:14.0	18.0		
XMM03153	0109520101	2002-01-29T08:46:18.0	26.6	104.7	375
	0210490101	2005-01-01T19:07:51.0	107.5		

Table A1. The X-ray observations log of our DOGs.

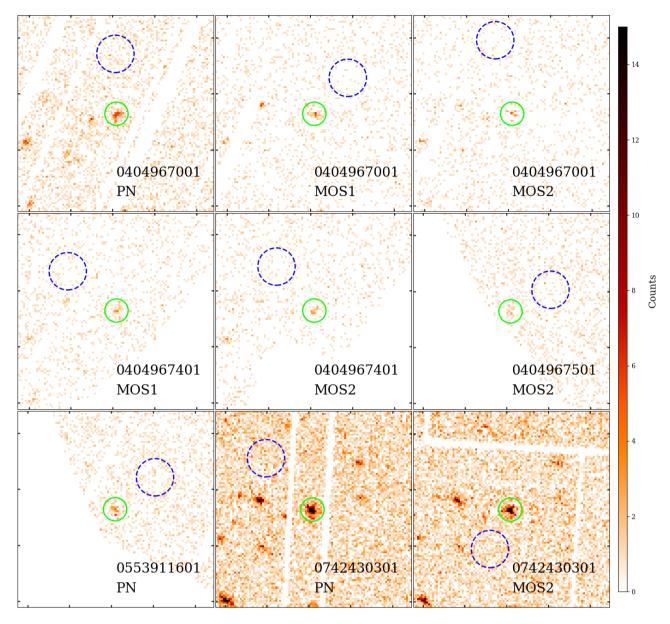| XID	Obs ID	Obs Date	$T_{\rm obs}$	Total $T_{\rm exp}^{\rm eff}$	Total Counts$_{(0.5-10\ {\rm keV})}$
		(YYYY-MM-DD:Thh:mm:ss)	(ks)	(ks)	(cts)
(1)	(2)	(3)	(4)	(5)	(6)
XMM03342	0109520101	2002-01-29T08:46:18.0	26.6	62.8	61
	0112680301	2003-01-19T04:19:09.0	23.4		
	0210490101	2005-01-01T19:07:51.0	107.5		
	6390 (Ch)	2005-09-13T21:44:12	11.9		
	7182 (Ch)	2005-10-12T03:55:24	22.9		
	6394 (Ch)	2005-10-12T22:57:34	17.5		
	7184 (Ch)	2005-10-14T19:16:55	22.7		
	7183 (Ch)	2005-10-15T14:18:10	19.9		
	7185 (Ch)	2005-11-21T09:59:42	32.9		
XMM03798	0112680301	2003-01-19T04:19:09.0	23.4	55.6	170
	0210490101	2005-01-01T19:07:51.0	107.5		
	0780450701	2016-08-14T19:39:55.0	17.9		
	0780451101	2017-01-07T10:58:53.0	20.9		
XMM03900	0112681001	2002-01-30T16:49:27.0	41.8	72.0	661
	0112680301	2003-01-19T04:19:09.0	23.4		
	0780450701	2016-08-14T19:39:55.0	17.9		
	0780451101	2017-01-07T10:58:53.0	20.9		
XMM03916	0112681001	2002-01-30T16:49:27.0	41.8	40.2	96
	0780450601	2016-08-14T14:36:35.0	17.0		
	0780450701	2016-08-14T19:39:55.0	17.9		
	0780451001	2017-01-07T04:50:33.0	20.9		
	6864 (Ch)	2006-11-12T05:00:26	29.7		
XMM04259	0109520301	2002-02-02T11:26:13.0	22.6	51.9	103
	0780451001	2017-01-07T04:50:33.0	20.9		
	0780451301	2017-01-08T18:27:03.0	20.0		
	0780451401	2017-01-09T00:20:23.0	20.0		
	0780452601	2017-02-10T05:38:28.0	16.0		
	9368 (Ch)	2007-11-23T16:55:22	75.0		
	18264 (Ch)	2016-09-27T19:47:17	22.8		
XMM04404	0112680101	2002-01-28T23:39:09.0	30.2	47.0	238
	0112680201	2002-07-14T02:10:42.0	21.6		
	0780451501	2017-01-09T06:13:43.0	20.0		
	0780451601	2017-01-09T12:07:03.0	36.4		
	0780451701	2017-01-10T19:11:08.0	20.0		
XMM04475	0109520201	2002-01-29T16:53:38.0	25.6	101.9	131
	0109520301	2002-02-02T11:26:13.0	22.6		
	0112681301	2002-07-26T08:26:58.0	40.4		
	0780451301	2017-01-08T18:27:03.0	20.0		
	0780451401	2017-01-09T00:20:23.0	20.0		
	0780452101	2017-01-13T09:20:32.0	20.0		
	0780452601	2017-02-10T05:38:28.0	16.0		
	9368 (Ch)	2007-11-23T16:55:22	75.0		
XMM04583	0404964801	2006-07-07T11:42:54.0	11.9	67.8	255
	0404964901	2006-07-07T15:39:35.0	11.7		
	0404969201	2006-07-26T20:57:30.0	7.9		
	0553910401	2008-08-06T22:19:42.0	11.9		
	0785102401	2016-08-12T12:23:12.0	22.0		
	0785102501	2016-08-12T18:49:52.0	22.0		
	0793581601	2017-01-05T08:26:38.0	9.0		
XMM04804	0112680401	2002-02-02T18:26:41.0	24.9	60.2	151
	0112681301	2002-07-26T08:26:58.0	40.4		
	0780451801	2017-01-11T01:04:28.0	20.0		
	0780452101	2017-01-13T09:20:32.0	20.0		
XMM04899	0109520201	2002-01-29T16:53:38.0	25.6	49.7	257
	0780451901	2017-01-11T06:57:48.0	20.0		
	0780452101	2017-01-13T09:20:32.0	20.0		

Figure A1. The *XMM-Newton* pn and MOS images of XMM00267 from different epochs (observation IDs). The source and background extraction regions are shown with green solid circles and blue dotted circles, respectively. The epochs (observation IDs) in which the target source fell outside the CCD or in the CCD gaps were discarded. The vertical colour bar indicates total counts in the 0.5−10 keV band. As expected, images from observation ID 0742430301 with a much higher exposure time of 100 ks show a lot more counts. The extraction regions on XMM00276 images are shown here as an example case, and the same strategy is followed for other sample sources.
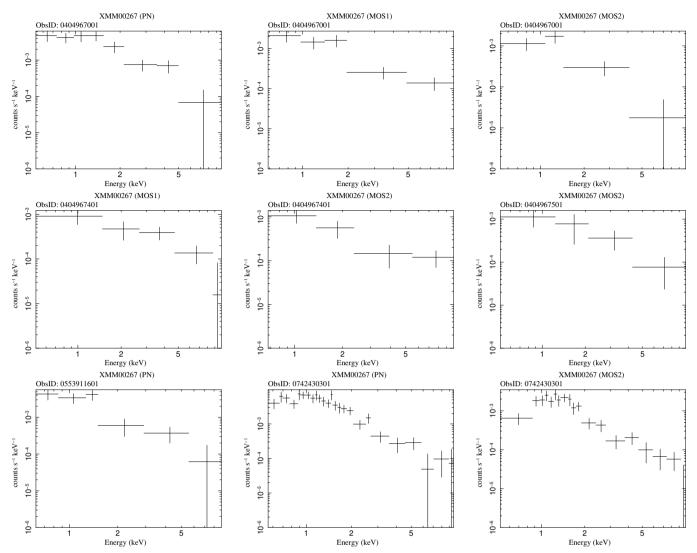
Figure A2. The 0.5−10 keV *XMM-Newton* pn and MOS background-subtracted source spectra of XMM00267 were extracted from the individual images of different epochs (observation IDs). The corresponding images are shown in Figure A1. For better visualisation, all spectra are rebinned by 10 counts per bin. The XMM00267 spectra are shown here to present an example case.
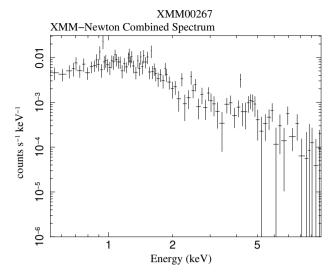
Figure A3. The 0.5−10 keV *XMM-Newton* spectrum obtained by combining pn, MOS1 and MOS2 spectra of all epochs (observation IDs) of XMM00267. The combined spectrum of XMM00267 is shown here as an example case and the same strategy is followed for other sample sources.
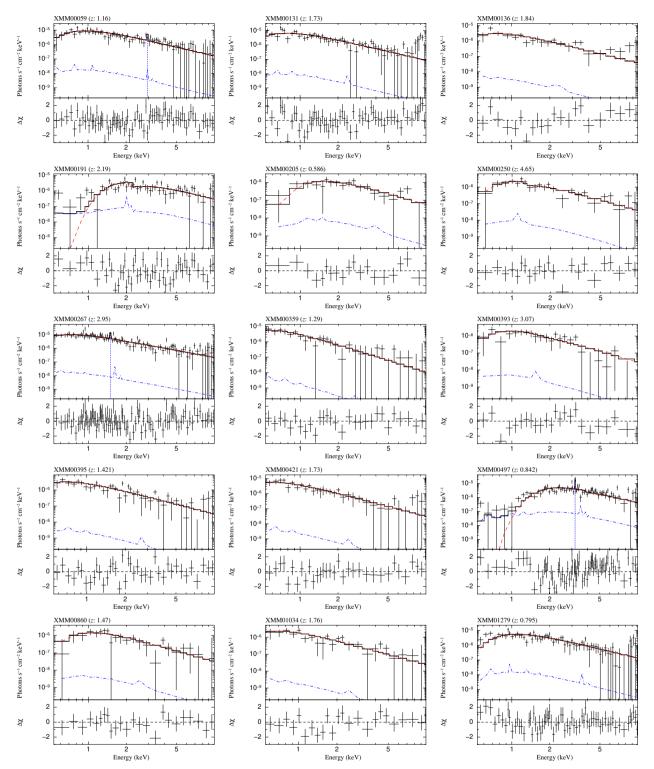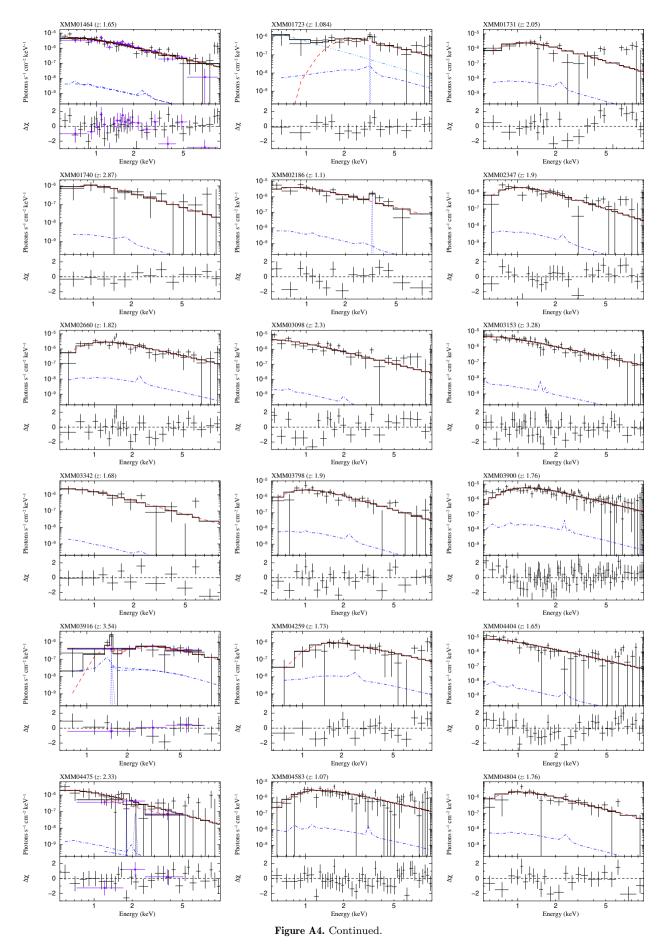
Figure A4. The $0.5 - 10$ keV unfolded X-ray spectra of our DOGs best-fitted with BORUS02 model. For better visualisation, spectra are rebinned with 10 counts per bin. The best-fitted model is shown with a solid black curve, and model components, *i.e.,* cutoff power law, scattered cutoff power law and reflection component, are shown with a red dashed curve, cyan dash tipple-dotted curve and blue dash-dotted curve, respectively. The Fe Kα line is shown by a blue narrow Gaussian. The XMM-Newton and *Chandra* data points are shown with black crosses and purple empty circles, respectively. The bottom panels in each sub-figure show residuals.

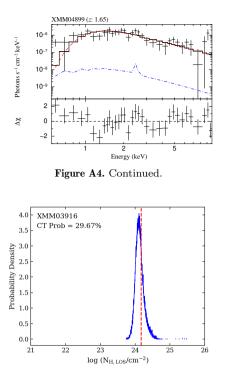**Figure A4.** Continued.

Figure A4. Continued.

Figure A5. The MCMC-based N_{H} probability distribution function (PDF) of the CT-AGN candidate XMM03916. The best fits using the BORUS02 model are used to derive N_{H} PDFs. The red dashed vertical line shows the Compton-thick limit of $N_{\mathrm{H}} = 1.5 \times 10^{24}$ cm^{-2}.

Table A2. The best-fitted X-ray fluxes and luminosities using absorbed power law and borus02 models.

XID	ABSPOW			BORUS02			$\log L_{6\ \mu m}$	$\lambda_{\rm Edd}$
	$\log F_{2-10\ \rm keV}$ (erg cm^{-2} s^{-1})	$\log L^{\rm obs}_{2-10\ \rm keV}$ (erg s^{-1})	$\log L^{\rm int}_{2-10\ \rm keV}$ (erg s^{-1})	$\log F_{2-10\ \rm keV}$ (erg cm^{-2} s^{-1})	$\log L^{\rm obs}_{2-10\ \rm keV}$ (erg s^{-1})	$\log L^{\rm int}_{2-10\ \rm keV}$ (erg s^{-1})	(erg s^{-1})	
(1)	(2)	(3)	(4)	(5)	(6)	(7)	(8)	(9)
XMM00059	$-13.34^{+0.04}_{-0.04}$	$44.48^{+0.04}_{-0.04}$	$44.54^{+0.05}_{-0.05}$	$-13.36^{+0.04}_{-0.04}$	$44.48^{+0.04}_{-0.04}$	$44.51^{+0.03}_{-0.03}$		$0.18^{+0.39}_{-0.12}$
XMM00131	$-13.64^{+0.06}_{-0.06}$	$44.61^{+0.04}_{-0.05}$	$44.70^{+0.06}_{-0.06}$	$-13.65^{+0.06}_{-0.06}$	$44.61^{+0.04}_{-0.06}$	$44.65^{+0.04}_{-0.04}$	45.11	$0.27^{+0.58}_{-0.18}$
XMM00136	$-14.02^{+0.08}_{-0.09}$	$44.30^{+0.07}_{-0.07}$	$44.39^{+0.09}_{-0.09}$	$-14.03^{+0.08}_{-0.08}$	$44.30^{+0.07}_{-0.07}$	$44.34^{+0.06}_{-0.07}$	45.70	$0.11^{+0.25}_{-0.08}$
XMM00191	$-13.21^{+0.06}_{-0.07}$	$44.77^{+0.05}_{-0.06}$	$45.49^{+0.08}_{-0.09}$	$-13.22^{+0.08}_{-0.06}$	$44.78^{+0.04}_{-0.05}$	$45.59^{+0.05}_{-0.05}$		$4.59^{+9.92}_{-3.14}$
XMM00205	$-13.86^{+0.11}_{-0.10}$	$43.24^{+0.09}_{-0.09}$	$43.30^{+0.13}_{-0.11}$	$-13.86^{+0.11}_{-0.10}$	$43.24^{+0.09}_{-0.09}$	$43.30^{+0.13}_{-0.11}$	44.84	$0.01^{+0.02}_{-0.01}$
XMM00250	$-13.96^{+0.09}_{-0.10}$	$44.89^{+0.08}_{-0.09}$	$45.43^{+0.10}_{-0.10}$	$-13.99^{+0.09}_{-0.17}$	$44.89^{+0.08}_{-0.09}$	$45.52^{+0.06}_{-0.07}$	46.22	$3.67^{+7.93}_{-2.51}$
XMM00267	$-13.35^{+0.07}_{-0.08}$	$45.27^{+0.11}_{-0.03}$	$45.38^{+0.06}_{-0.06}$	$-13.35^{+0.07}_{-0.08}$	$45.27^{+0.03}_{-0.03}$	$45.39^{+0.07}_{-0.06}$	45.57	$2.43^{+5.25}_{-1.66}$
XMM00359	$-14.36^{+0.28}_{-0.12}$	$43.80^{+0.14}_{-0.10}$	$43.84^{+0.19}_{-0.10}$	$-14.36^{+0.07}_{-0.11}$	$43.85^{+0.08}_{-0.15}$	$43.86^{+0.07}_{-0.10}$	45.13	$0.03^{+0.07}_{-0.02}$
XMM00393	$-14.09^{+0.20}_{-0.24}$	$44.63^{+0.07}_{-0.16}$	$44.94^{+0.27}_{-0.20}$	$-14.10^{+0.20}_{-0.24}$	$44.63^{+0.06}_{-0.23}$	$44.90^{+0.31}_{-0.22}$	45.62	$0.55^{+1.18}_{-0.37}$
XMM00395	$-14.05^{+0.07}_{-0.07}$	$44.01^{+0.06}_{-0.06}$	$44.07^{+0.07}_{-0.08}$	$-14.04^{+0.06}_{-0.04}$	$44.04^{+0.06}_{-0.07}$	$44.06^{+0.05}_{-0.05}$	44.87	$0.05^{+0.12}_{-0.04}$
XMM00421	$-13.99^{+0.08}_{-0.08}$	$44.32^{+0.07}_{-0.07}$	$44.34^{+0.08}_{-0.09}$	$-14.03^{+0.16}_{-0.20}$	$44.32^{+0.07}_{-0.13}$	$44.34^{+0.07}_{-0.07}$	44.53	$0.11^{+0.25}_{-0.08}$
XMM00497	$-12.94^{+0.04}_{-0.04}$	$44.38^{+0.03}_{-0.08}$	$44.70^{+0.05}_{-0.08}$	$-12.96^{+0.05}_{-0.03}$	$44.38^{+0.03}_{-0.03}$	$44.70^{+0.03}_{-0.03}$	45.24	$0.31^{+0.66}_{-0.21}$
XMM00860	$-14.08^{+0.23}_{-0.14}$	$43.97^{+0.09}_{-0.10}$	$44.11^{+0.15}_{-0.13}$	$-14.09^{+0.23}_{-0.25}$	$43.97^{+0.09}_{-0.27}$	$44.06^{+0.08}_{-0.09}$	45.03	$0.05^{+0.12}_{-0.04}$
XMM01034	$-14.20^{+0.10}_{-0.11}$	$44.09^{+0.08}_{-0.09}$	$44.15^{+0.10}_{-0.10}$	$-14.21^{+0.07}_{-0.07}$	$44.07^{+0.07}_{-0.07}$	$44.10^{+0.07}_{-0.08}$	44.87	$0.06^{+0.13}_{-0.04}$
XMM01279	$-13.49^{+0.05}_{-0.06}$	$43.96^{+0.05}_{-0.05}$	$44.01^{+0.06}_{-0.06}$	$-13.45^{+0.04}_{-0.04}$	$43.99^{+0.04}_{-0.04}$	$44.02^{+0.04}_{-0.04}$	44.46	$0.05^{+0.11}_{-0.03}$
XMM01464	$-13.87^{+0.10}_{-0.10}$	$44.33^{+0.05}_{-0.05}$	$44.37^{+0.06}_{-0.06}$	$-13.92^{+0.09}_{-0.09}$	$44.33^{+0.05}_{-0.07}$	$44.43^{+0.06}_{-0.07}$	44.78	$0.14^{+0.31}_{-0.10}$
XMM01723	$-13.73^{+0.12}_{-0.14}$	$43.82^{+0.09}_{-0.10}$	$44.19^{+0.26}_{-0.24}$	$-13.75^{+0.11}_{-0.14}$	$43.83^{+0.09}_{-0.10}$	$44.19^{+0.12}_{-0.15}$	43.17	$0.08^{+0.16}_{-0.05}$
XMM01731	$-14.00^{+0.35}_{-0.48}$	$44.46^{+0.09}_{-0.11}$	$44.73^{+0.37}_{-0.20}$	$-14.01^{+0.35}_{-0.19}$	$44.46^{+0.10}_{-0.30}$	$44.69^{+0.08}_{-0.09}$	45.76	$0.30^{+0.65}_{-0.20}$
XMM01740	$-14.33^{+0.20}_{-0.23}$	$44.33^{+0.14}_{-0.17}$	$44.55^{+0.22}_{-0.24}$	$-14.34^{+0.11}_{-0.17}$	$44.33^{+0.14}_{-0.17}$	$44.51^{+0.14}_{-0.17}$	45.67	$0.18^{+0.39}_{-0.12}$
XMM02186	$-13.86^{+0.11}_{-0.11}$	$43.93^{+0.09}_{-0.10}$	$43.98^{+0.11}_{-0.12}$	$-13.86^{+0.07}_{-0.08}$	$43.94^{+0.08}_{-0.08}$	$43.98^{+0.08}_{-0.08}$		$0.04^{+0.10}_{-0.03}$
XMM02347	$-14.03^{+0.09}_{-0.10}$	$44.25^{+0.07}_{-0.08}$	$44.41^{+0.10}_{-0.10}$	$-14.04^{+0.09}_{-0.10}$	$44.25^{+0.07}_{-0.08}$	$44.37^{+0.10}_{-0.11}$	44.77	$0.12^{+0.27}_{-0.08}$
XMM02660	$-13.70^{+0.07}_{-0.08}$	$44.52^{+0.06}_{-0.06}$	$44.70^{+0.08}_{-0.09}$	$-13.64^{+0.05}_{-0.06}$	$44.52^{+0.06}_{-0.06}$	$44.68^{+0.06}_{-0.06}$	45.44	$0.29^{+0.63}_{-0.20}$
XMM03098	$-14.15^{+0.10}_{-0.11}$	$44.43^{+0.07}_{-0.08}$	$44.49^{+0.10}_{-0.11}$	$-14.15^{+0.10}_{-0.06}$	$44.43^{+0.07}_{-0.07}$	$44.46^{+0.07}_{-0.07}$	45.46	$0.16^{+0.34}_{-0.11}$
XMM03153	$-13.87^{+0.11}_{-0.12}$	$44.88^{+0.04}_{-0.05}$	$44.99^{+0.10}_{-0.09}$	$-13.87^{+0.10}_{-0.12}$	$44.88^{+0.03}_{-0.13}$	$44.92^{+0.04}_{-0.04}$	46.17	$0.58^{+1.26}_{-0.40}$
XMM03342	$-14.41^{+0.38}_{-0.42}$	$43.91^{+0.13}_{-0.36}$	$43.98^{+0.25}_{-0.18}$	$-14.49^{+0.25}_{-0.18}$	$43.91^{+0.14}_{-0.17}$	$43.94^{+0.11}_{-0.13}$	45.40	$0.04^{+0.09}_{-0.03}$
XMM03798	$-13.99^{+0.19}_{-0.23}$	$44.40^{+0.06}_{-0.13}$	$44.61^{+0.15}_{-0.15}$	$-13.99^{+0.19}_{-0.15}$	$44.40^{+0.05}_{-0.10}$	$44.56^{+0.06}_{-0.07}$	45.72	$0.21^{+0.45}_{-0.14}$
XMM03900	$-13.40^{+0.05}_{-0.05}$	$44.78^{+0.04}_{-0.04}$	$44.97^{+0.06}_{-0.04}$	$-13.41^{+0.05}_{-0.05}$	$44.78^{+0.04}_{-0.04}$	$44.93^{+0.04}_{-0.04}$	45.26	$0.60^{+1.29}_{-0.41}$
XMM03916	$-13.74^{+0.13}_{-0.14}$	$44.29^{+0.20}_{-0.26}$	$45.48^{+0.14}_{-0.16}$	$-13.75^{+0.12}_{-0.14}$	$44.30^{+0.13}_{-0.14}$	$45.79^{+0.12}_{-0.14}$	46.32	$8.77^{+18.96}_{-6.00}$
XMM04259	$-13.81^{+0.18}_{-0.22}$	$44.15^{+0.18}_{-0.09}$	$44.48^{+0.33}_{-0.25}$	$-13.81^{+0.22}_{-0.15}$	$44.15^{+0.09}_{-0.10}$	$44.46^{+0.09}_{-0.10}$	45.31	$0.16^{+0.34}_{-0.11}$
XMM04404	$-13.77^{+0.06}_{-0.07}$	$44.42^{+0.08}_{-0.09}$	$44.45^{+0.08}_{-0.09}$	$-13.80^{+0.06}_{-0.07}$	$44.42^{+0.06}_{-0.07}$	$44.45^{+0.06}_{-0.07}$	45.33	$0.15^{+0.33}_{-0.10}$
XMM04475	$-14.38^{+0.13}_{-0.15}$	$44.26^{+0.09}_{-0.14}$	$44.28^{+0.17}_{-0.18}$	$-14.37^{+0.12}_{-0.11}$	$44.26^{+0.07}_{-0.18}$	$44.29^{+0.10}_{-0.12}$	44.96	$0.10^{+0.21}_{-0.07}$
XMM04583	$-13.58^{+0.08}_{-0.09}$	$44.12^{+0.07}_{-0.07}$	$44.25^{+0.08}_{-0.09}$	$-13.59^{+0.08}_{-0.09}$	$44.11^{+0.07}_{-0.07}$	$44.21^{+0.06}_{-0.06}$		$0.08^{+0.17}_{-0.05}$
XMM04804	$-13.95^{+0.18}_{-0.22}$	$44.28^{+0.07}_{-0.07}$	$44.44^{+0.14}_{-0.12}$	$-13.95^{+0.06}_{-0.07}$	$44.28^{+0.07}_{-0.07}$	$44.39^{+0.06}_{-0.07}$	43.18	$0.13^{+0.28}_{-0.09}$
XMM04899	$-13.76^{+0.08}_{-0.08}$	$44.29^{+0.06}_{-0.05}$	$44.56^{+0.08}_{-0.09}$	$-13.77^{+0.04}_{-0.07}$	$44.29^{+0.06}_{-0.06}$	$44.53^{+0.05}_{-0.06}$	44.88	$0.19^{+0.41}_{-0.13}$

Notes - The X-ray fluxes and errors are obtained using the 'cflux' command in the xspec. The observed and absorption-corrected X-ray luminosities and errors are obtained using the 'clumin' command in the xspec. The 6.0 μm luminosities are gleaned from Zou et al. (2022), who derived them from the broad-band SED modelling. The large error bars introduced in $\lambda_{\rm Edd}$ correspond to the assumed one dex spread ($10^8 - 10^9\ M_\odot$) in $M_{\rm BH}$.